Article

Clay mineralogical evidence of near-equatorial Palaeocene–Eocene Thermal Maximum in Barmer Basin, India

Rohit Kumar 🔟, Abdul Hameed 🔟 and Pankaj Srivastava 🔟

Department of Geology, University of Delhi, Delhi 110007, India

Abstract

The Palaeocene–Eocene Thermal Maximum (PETM) was a global extreme climatic event, but it is relatively unknown from lower latitudes or equatorial regions in comparison to mid- and high latitudes. The present study provides the first clay mineralogical evidence of the PETM and subsequent hyperthermal events in a near-equatorial region represented by the Akli Formation in the Barmer Basin, India. The 32 m-thick succession of the Akli Formation shows abrupt changes in smectite and kaolin abundances preceding, during and succeeding the PETM event. Within the studied section, the kaolin content increases from 5–8% pre-PETM to 30–35% during the PETM, and then again decreases to 5–6% during the post-PETM period. The smectite, however, is marked by a corresponding decrease and its transformation into kaolin in acid weathering conditions. The transformation of the smectite is first marked by hydroxy interlayering and then transformation into kaolin during the PETM. The transformation of smectite into kaolin also resulted in extensive precipitation of iron oxide in sediments. The clay mineralogical changes in the Palaeocene–Eocene transition sediments of the Akli Formation were caused by 3–5°C warming and a 25–50% increase in rainfall during the hyperthermal events. Unusually high charcoal (~20%) fragments during the Palaeocene–Eocene transition also suggest warming and widespread biomass burning during the PETM in the lower latitudes.

The Cenozoic record of Earth's history is marked by the major shift from greenhouse to icehouse conditions. The Palaeocene–Eocene Thermal Maximum (PETM) at ~56 Ma is regarded as one of the most profound global warming events during the Cenozoic that released carbon comparable to modern sources (Zachos *et al.*, 2001; Rohl *et al.*, 2007; Westerhold *et al.*, 2009; Murphy *et al.*, 2010). The global marine and terrestrial record of the warming during the Palaeocene–Eocene (P–E) transition clearly shows five transient hyperthermal events that are marked by negative carbon isotope excursions (CIEs), namely the PETM, the Eocene Thermal Maximum 2 (ETM2) or H1 and three others known as H2, I1 and I2. Of these events, the first two (i.e. PETM and ETM2) are the major CIEs, whereas the others demarcate minor CIEs (Dickens *et al.*, 1995, 1997; Westerhold *et al.*, 2020). Over a short interval of 150,000 years during the PETM, the average global temperature rose by 5–10°C together with acidification of the oceans and abrupt change in the hydrological cycle (Wing *et al.*, 2005; Zachos *et al.*, 2005; Röhl *et al.*, 2007; Secord *et al.*, 2010; Cui *et al.*, 2011; McInerney & Wing, 2011).

Over the last few decades, the PETM and the subsequent hyperthermal events have been reported on extensively, but mainly with regards to mid-range and high latitudes. These hyperthermal events influenced the marine and terrestrial

ecosystems of the Earth significantly (Kennett & Scott, 1991; Koch *et al.*, 1992; Zachos *et al.*, 2003, 2006; Smith *et al.*, 2007; Elling *et al.*, 2019). For example, the warming during the P–E transition resulted in a rapid depletion of the $\delta^{13}C$ (–3‰ to –4‰), acidification of the oceans, changes in the ocean circulation, and the benthic extinction in the marine realm (Kennett & Scott, 1991).

The terrestrial sedimentary record of the Earth is also marked by enhanced silicate weathering and an abundance of kaolinite (Ka) in P–E transition sediments, with examples from the North Sea Basin of Europe, the Tethys Sea, north-west Argentina, sections of the Bass River and Williston Basin in the USA (Cramer *et al.*, 1999, Bolle & Adatte, 2001, Clechenko *et al.*, 2007; Kemp *et al.*, 2016; Do Campo *et al.*, 2018). The terrestrial record of the Qaidam Basin, north-west China, has been explored for clay mineralogical details of the Early Eocene Climate Optimum (EECO) in the interval 53–49 Ma, which also confirmed elevated temperatures and increased chemical weathering controlled by global climatic changes (Wang *et al.*, 2011; Zhao *et al.*, 2021). The Bighorn Basin in the USA is marked by contrasting results in comparison to the nearby Williston Basin, as it is characterized by the dominance of physical weathering and erosion over chemical weathering (Wang *et al.*, 2017; Ji *et al.*, 2023).

The terrestrial sedimentary record of the PETM reported from various parts of the world shows a close correspondence and equivalence with marine records (Koch *et al.*, 1992). For example, the palaeosols that formed during the P–E transition are also marked by warming, increased chemical weathering and depletion

of $\delta^{13}C$ similar to marine records (Koch *et al.*, 1992). Biotic life across the continents was also influenced by the rapid warming during the P–E transition and is characterized by a dramatic shift in the vegetation from a mixed angiosperm–conifer flora to a purely angiosperm flora (Pagani *et al.*, 2006; Schouten *et al.*, 2007; Smith *et al.*, 2007).

In light of the available terrestrial record of the PETM and EECO, it is necessary to address the critical issues regarding research into the P–E transition warming: (1) most of the reports on the PETM and subsequent hyperthermals are mainly from high latitudes, but there is less research exploring the lower latitudes and equatorial regions of the past (Jaramillo, 2002; Handley *et al.*, 2012; Frieling *et al.*, 2017, 2018); (2) despite there being valuable information about the PETM and subsequent hyperthermals at the global level, information on the tropical regions remains limited; (3) the exact causal relationship regarding the warming between the lower and higher latitudes is still far from completely understood; (4) the possible similarities or differences in warming, wetting and increases in weathering at the higher and lower latitudes are not known; (5) clay mineral responses to weathering during hyperthermals in the palaeotropics are not known; and (6) there are many reports that indicate P–E hyperthermals are similar to modern increases in temperature and pCO_2 in the atmosphere, but in the lower latitudes this information is still not known.

Thus, it is necessary to address such issues using various proxies and to unravel the physical, chemical and biological details of the PETM from the lower latitudes and the equatorial regions of the past. A detailed understanding of the PETM and subsequent warming events in lower latitudes is crucial to define the pole-to-equatorial gradient of the temperature increase, the latitudinal variation of the pCO_2 forcing and the extent and intensity of chemical weathering on the surface of the Earth. Therefore, the present study of Akli Formation sediments is of great importance because it represents a near-equatorial location during the P–E transition period. The main objective of the present study is to explore the clay mineralogy of the P–E transient sediments showing extreme climatic conditions at 150–200 ky intervals and to test the responses of clay minerals to intense climatic stress at the global level. In this study, we have used detailed clay mineralogy to explore the PETM and subsequent hyperthermal events in a 32 m-thick succession of the Akli Formation, Barmer Basin. This work highlights the PETM details of near-equatorial regions in the past in terms of clay mineralogical changes and their relationship with increased chemical weathering, warming and wetting in the equatorial region of the past. Furthermore, this work on clay mineral evidence from the PETM provides a valuable addition to the available biotic and carbon isotopic evidence of the hyperthermals recorded in the Himalayas and western India (Prasad *et al.*, 2009; Samanta *et al.*, 2013; Sreenivasan *et al.*, 2018; Gupta & Kumar, 2019; Khozyem *et al.*, 2021; Choudhury *et al.*, 2021).

Materials and methods

Geological setting of the study area

The Barmer Basin constitutes a part of the West Indian Rift System (WIRS) and is critical to understanding the tectonic and geological evolutionary history of the WIRS (Biswas, 1982; Gombos *et al.*, 1995; Compton, 2009; Bladon *et al.*, 2015). The Barmer Basin is a failed continental rift basin 200 km long,

40 km wide and 6 km deep (Fig. 1). It is filled with fluvial, lacustrine and marine-influenced sediments of Neoproterozoic to Cenozoic age (Dasgupta, 1974; Tripathi *et al.*, 2003, 2009; Bladon *et al.*, 2015). The pre-rift sediments include the Neoproterozoic–Early Cambrian of Birmania Formation and the Jurassic Lathi and Jaisalmer formations. The Sarnu, Barmer and Fatehgarh formations are the syn-rift sediments that were deposited during the Cretaceous period. Finally, the Mata-Ji-ka Dunger Formation and the Akli Formation are the post-rift sediments of the Palaeogene period (Dasgupta, 1974; Tripathi *et al.*, 2003, 2009).

The geological setting of the Barmer Basin shows that sediments of the Akli Formation were mainly sourced from the Malani Igneous Suite (Fig. 1). The igneous suite of ~750 Ma consists mainly of an extrusive phase of rhyolitic rocks and stratified tuffs that were later intruded by granite and rhyolitic porphyry dykes (Eby & Kochhar, 1990; Maheshwari *et al.*, 2001; Gregory *et al.*, 2009). The extrusive rhyolitic phase is generally aphyric in nature, with a few phenocrysts of quartz (Q) and K-feldspar (Eby & Kochhar, 1990; Maheshwari *et al.*, 2001).

The P–E transition sediments of the Akli Formation, Barmer Basin, are ~265 m thick and overlie the Mata-Ji-ka Dunger Formation in the uppermost part of the Barmer Basin (Fig. 1). The Giral mine (26°04′ N latitude, 71°16′ E longitude) exposes the best representative section of the Akli Formation and has been studied extensively for pollen and vertebrate fauna (Tripathi *et al.*, 2003; Rana *et al.*, 2005). The Giral mine section comprises a 32 m-thick succession of alternating bands of bentonite, carbonaceous clay, grey to reddish clay and lignite (Tripathi *et al.*, 2003, 2009; Rana *et al.*, 2005). The palynological and vertebrate palaeontological evidence suggests that the Akli Formation sediments were deposited in coastal floodplains with frequent marine excursions and mangrove-dominated vegetation of the tropics (Naskar & Baksi, 1976; Pareek, 1981, 1984; Tripathi *et al.*, 2003, 2009; Rana *et al.*, 2006; Singh, 2015; Nagori & Khosla, 2019; Prasad *et al.*, 2020; Khozyem *et al.*, 2021).

The sedimentological features of the 32 m section of the Giral mine section show that it comprises horizontally bedded metre-scale lignite, clay, silty clay, silty loam, sandy loam and fine sand beds (Fig. 2 & Table 1). The lignite beds occur mainly in the lowermost parts (L1 and L2) and are followed by 24 beds of clay, silty clay, silty loam, sandy loam and fine sand and thin lignite units. The clay, silty clay and silty loam units constitute a major part (i.e. ~25.5 m in bed nos. 1–3, 6–7 and 8–24), whereas the sandy loam and fine sand units constitute only up to ~3 m (i.e. bed nos. 4, 5 and 7) at 18–22 m depth of the section (Fig. 2). The beds are either laminated or massive and are defined by varying thicknesses, textures, colours and varying abundances of gypsum and charcoal (Table 1). The silty clay bed nos. 7, 11, 13 and 23 at 17, 12, 9 and 0.5 m depths, respectively, are characterized by millimetre-scale laminations of light and dark colours, whereas all other beds are massive (Table 1).

Age constraints

The palynological assemblage, vertebrate fauna and $\delta^{13}C$ curve of the studied section and their global correlation provide the age constraints of the Akli Formation. The palynological evidence from the Akli Formation is comparable to P–E assemblages of India and elsewhere (Naskar & Baksi, 1976; Tripathi 1993, 1995, 1997; Tabaei & Singh, 2002; Tripathi *et al.*, 2003, 2009; Singh, 2015; Khanolkar & Sharma, 2019). The palynological assemblages of the Akli Formation were used to establish two
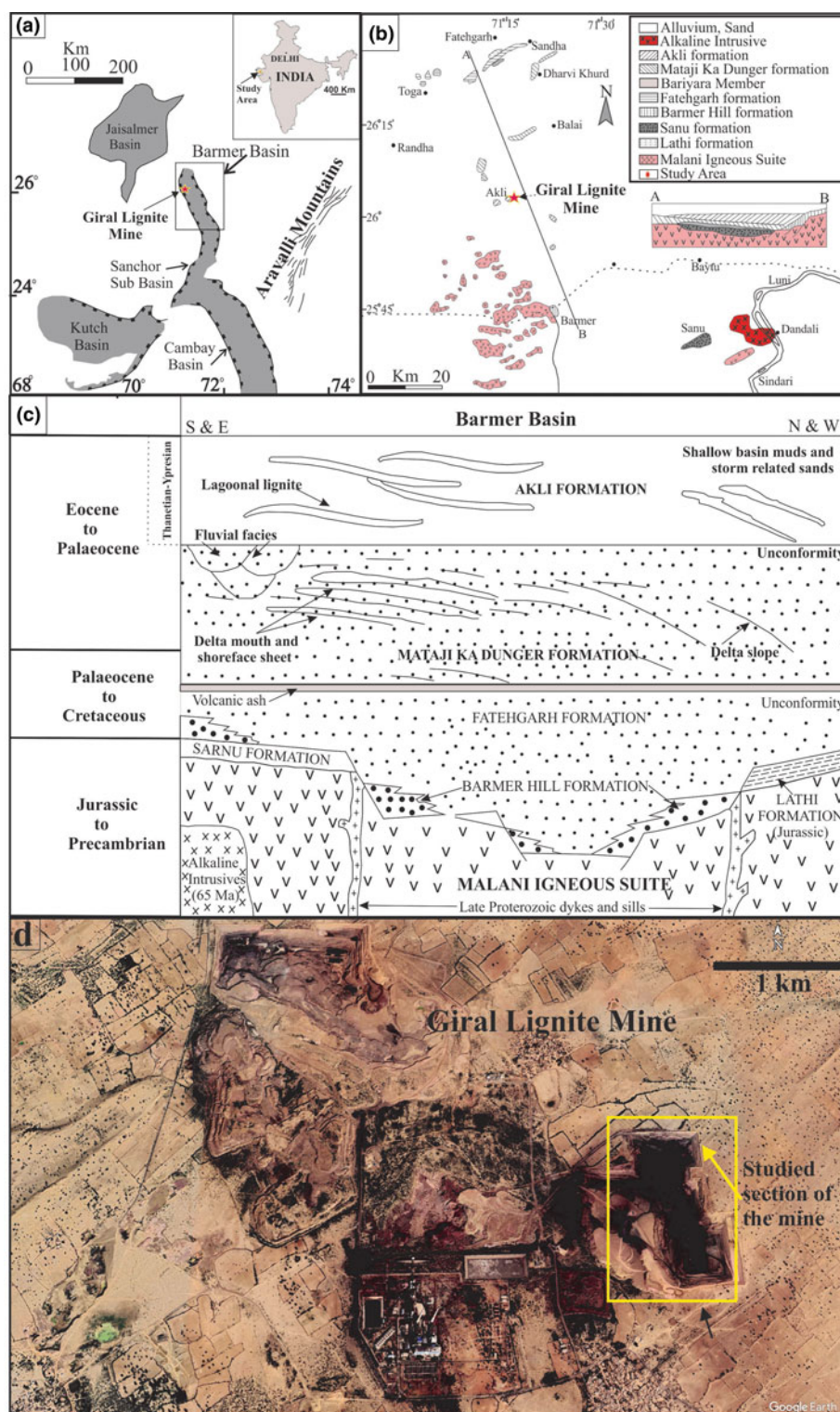
Figure 1. (a) Rift basins of western India (after Bladon et al., 2015) and location of the Giral lignite mine in Barmer Basin. (b) Geological map of the Barmer Basin and location of the Giral lignite mine (after Sisodia & Singh, 2000). (c) Lithostratigraphy of the Barmer Basin (after Sisodia & Singh, 2000). (d) Google Earth image of the Giral lignite mine and the studied section.

informal palynozones demarcating late Palaeocene and Early Eocene sediments (Tripathi 1993, 1995, 1997; Tripathi et al., 2003, 2009). The two distinct palynozones are separated at ~20 m depth of the Giral mine section (Tripathi et al., 2003, 2009). The lower palynozone is defined by pteridophytic spores and dinoflagellate cysts consisting of the major taxa *Lygodiumsporites eocenicus*, *Todisporites kutchensis* and *Dandotiaspora dilata*, of which *Dandotiaspora* is considered to

be the most characteristic marker of the Palaeocene to Early Eocene age (Naskar & Baksi, 1976; Tripathi et al., 2003, 2009). The upper palynozone is characterized by angiosperm pollens consisting of *Spinizonocolpites echinatus*, *Matanomadhiasulcites microreticulatus*, *Proxaperites cursus*, *Proxaperites microreticulatus*, *Kapurdipollenites gemmatus* and *Retiverrumonosulcites barmerensis* (Tripathi et al., 2003, 2009). The lower palynozone assemblage indicates a Late Palaeocene
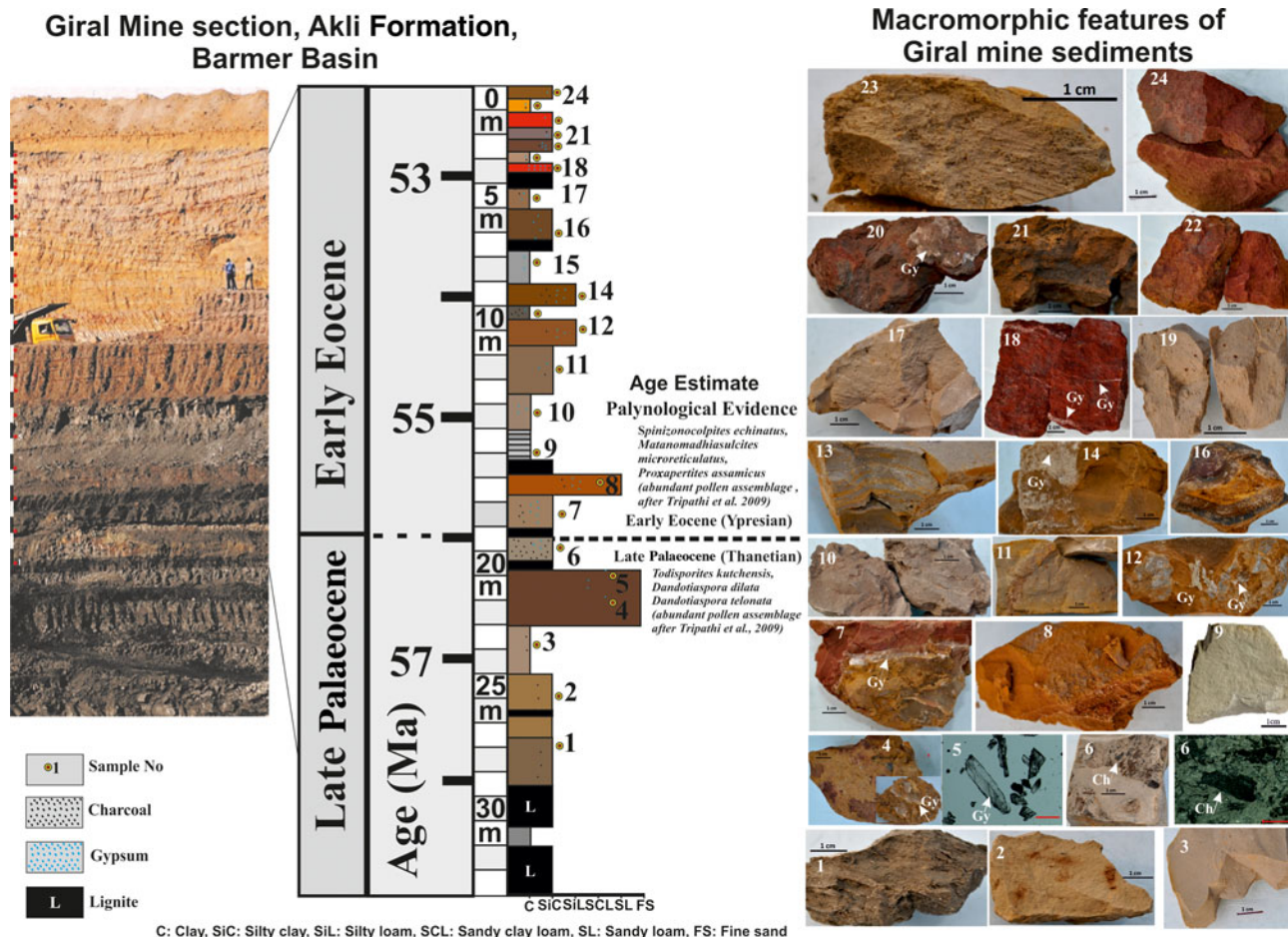
Figure 2. Lithology of the 32 m studied section of the Giral mine showing the P–E transition (age estimate based on Thanetian–Ypresian characteristic pollen assemblages) and 24 representative beds and their macroscopic features. The colour, texture, structure, charcoal (Ch) and gypsum (Gy) contents based on the present study are summarized in Table 1.

(Thanetian) age for these sediments as the assemblage either dwindles or disappears completely in the Early Eocene (Tripathi et al., 2003, 2009). The upper palynozone is typically characterized by species of *Spinizonocolpites*, an extinct *Nypa*-like pollen of palms of Early Eocene (Ypresian) age (Tripathi et al., 2003, 2009). *Nypa* pollens were the most widespread pollens globally during the Eocene, but the onset of cooling during the Late Eocene resulted in their decline and extinction (Morley, 2000; Pocknall et al., 2022). The presence of *Nypa* pollens in sediments indicates a mangrove environment in tidal mud flats (Chaloner, 1968; Morley, 2000; Pocknall et al., 2022).

The vertebrate fossils recovered from the Giral mine section and the adjoining lignite mines of the Barmer Basin and their global correlation also provide the age of the Akli Formation (Rana et al., 2005; Rose et al., 2006; Smith et al., 2016; Rajkumari & Prasad, 2020). The vertebrate fossils in the Giral and the adjoining mines support a Thanetian age for the lower palynozone of the Giral mine section (Rajkumari & Prasad, 2020). The vertebrate fauna of the Akli Formation show their wide palaeogeographical distribution in the Late Palaeocene sediments of the USA, Europe, Africa and Asia (Arambourg, 1952; Noubhani & Cappetta, 1997; Knight et al., 2007; Cappetta, 2012; Ebert & Stehmann, 2013; Rajkumari & Prasad, 2020).

The global reference curves of the carbon (δ^{13}C) and oxygen (δ^{18}O) isotope compositions of the benthic foraminifera

demonstrate sharp but negative shifts in the isotopes during the Palaeogene hyperthermals (Westerhold et al., 2020). The PETM and the subsequent Early Eocene hyperthermals (EECO) are defined by a sharp depletion of δ^{13}C up to –3‰ from background values (Westerhold et al., 2020). The δ^{13}C curves of the Giral mine sections and five neighbouring sections show a remarkable consistency with global reference curves (Westerhold et al., 2020; Khozyem et al., 2021). The high-resolution $\delta^{13}C_{org}$ data of the 32 m studied section is marked by a sharp depletion of approximately –3‰ at 19–22 m depth and then again a depletion of approximately –2.5‰ at 2–3 m depth (Khozyem et al., 2021). The δ^{13}C curve of the studied section is consistent with the global reference curve, and the depletion of δ^{13}C at 19–22 m depth defines the PETM at 56 Ma, whereas the next depletion of δ^{13}C at 2–3 m depth defines the ETM2 (Khozyem et al., 2021). Based on the above palaeontological evidence and the δ^{13}C curve, the studied Giral mine section of the Akli Formation represents P–E transition sediments and the ~20 m depth of the section represents the Late Palaeocene (Thanetian)–Early Eocene (Ypresian) boundary, providing an important archive of the Palaeogene hyperthermals.

Bulk mineralogical composition

The 32 m Giral mine section was explored at the site for macroscopic features such as the structure, texture, colour and thickness

Table 1. Macroscopic features of the 24 beds in the 32 m Giral mine section of the Akli Formation, Barmer Basin.

Sample no.	Depth (m)	Munsell colour	Texture	Gypsum (%)	Charcoal (%)	pH	Remarks
24	0.15	Dark brown (7.5 R 3/3)	Silty clay	<1	–	7.5	Deep red massive silty clay with few yellowish mottles
23	0.65	Light brownish-grey (2.5 Y 6/2)	Clay	<1	1–2	7.3	Light brown clay with very fine laminations and voids
22	1.10	Dusky red (7.5 R 3/4)	Silty clay	<1	–	7.4	Deep red massive silty clay with yellowish-orange mottles and biogenic activity
21	1.60	Dark yellowish-brown (10 YR 4/1)	Silty clay	<1	<1	7.5	Yellowish-brown massive silty clay with light yellow-orange mottles and organic matter
20	2.10	Dark reddish-brown (2.5 YR 3/4)	Silty clay	5–6	–	5.4	Deep red massive silty clay with few sand fillings, orange mottles and biogenic activity
19	2.75	Grey (10 YR 6/1)	Clay	<1	<1	5.3	Grey massive clay with reddish mottle and cavities, slickensides and biogenic activity
18	3.25	Dark red (7.5 R 3/6)	Silty clay	10–12	<1	5.1	Deep red massive silty clay with orange motels and many thin and dense gypsum layers
17	4.40	Grey (7.5 YR 6/1)	Clay	5–6	3–4	4.7	Grey massive clay with orange and red mottles along with gypsum in groundmass
16	5.75	Reddish-black (5R2.5/1)	Silty clay	4–5	–	4.4	Reddish-black massive silty clay with orange-red mottles and solution activity
15	7.50	Grey (7.5 YR 6/1)	Clay	4	3–4	4.6	Grey massive clay with reddish-orange mottles, slickensides and biogenic activity
14	8.50	Yellowish-brown (10 YR 5/4)	Silty loam	6–7	3–4	3.9	Deep orange to red massive silty loam with gypsum at surface and matrix
13	9.30	Grey (10 YR 6/1)	Clay	<1	4–5	4.5	Grey and yellowish laminated clay with solution activity
12	10.10	Brown (7.5 YR 4/4)	Silty loam	3–4	<1	3.5	Reddish-brown massive silty loam with slickensides and dense fibrous gypsum at surface
11	11.75	Grey (7.5 YR 5/1)	Silty clay	<1	1–2	3.6	Greyish-brown massive to laminated silty clay with orange mottles and burrowing activity
10	13.25	Reddish-grey (2.5 R 4/1)	Clay	3–4	<1	4.1	Grey massive silty clay with orange mottles and gypsum at surface
9	15.00	White (2.5 Y 8/1)	Clay	–	<1	4.1	White and light grey thin layers of clay with few orange mottles
8	16.00	Strong brown (7.5 YR 5/6)	Sandy loam	2–4	1–2	3.5	Strong brown to reddish massive sandy loam with gypsum in groundmass and surface
7	17.50	Greyish-brown (10YR 5/2)	Silty clay	5–6	4–5	4.3	Greyish-brown-red-orange laminated silty clay with thick and dense gypsum layer
6	19.00	Reddish-grey (2.5 YR 5/1)	Silty clay	3–4	15–20	6.9	Reddish-grey massive silty clay with abundant charcoal fragments
5	20.00	Dark reddish-brown (2.5 YR 3/4)	Fine sand	3–4	1–2	5.0	Reddish-brown fine sand and clay with thin layers of gypsum at surface and fracture zones
4	21.00	Dark reddish-brown (2.5 YR 2.5/4)	Fine sand	2–3	<1	5.1	Reddish-brown fine sand and clay with few gypsum grains at surface
3	23.00	Grey (7.5 YR 6/1)	Clay	–	<1	5.0	Grey massive clay with reddish mottles and slickensides
2	25.00	Light grey (2.5 Y 7/2)	Silty clay	–	2–3	7.7	Yellowish-grey massive silty clay with deep red mottles
1	27.00	Dark grey (2.5 Y 4/1)	Silty clay	–	3–4	6.0	Dark grey to brown massive silty clay with lots of organic matter and charcoal fragments
L1	28.50	Dark black	Lignite	–	–	–	Dark black to brown lignite layer
0	30.50	Grey (7.5 YR 6/1)	Clay	–	–	–	Grey massive clay with reddish mottles and slickensides
L2	31.20	Dark black	Lignite	–	–	–	Dark black to brown lignite layer

of beds/laminations and the presence of carbonates, charcoal, and gypsum to construct a lithology using standard procedures (Stow, 2005; Nichols, 2009). Representative samples from 24 different beds were used for clay mineralogical studies. The pH of all representative samples was measured using a 1:2 soil:water ratio (Jackson, 1975).

X-ray diffraction (XRD) was used for bulk mineralogy and clay mineralogy of total clay (TC; <2 μm) and fine clay (FC; <0.2 μm) fractions of all 24 representative samples (Jackson, 1975; Wilson, 1987). For bulk mineralogy, powdered samples (∼100 mesh) were analysed using XRD as a non-orientated powder with Cu-$K\alpha$ radiation in the range 3–70°2θ with a scanning speed of 1°2θ min^{-1} in continuous acquisition mode using a PANalytical X'Pert powder X-ray diffractometer (Malvern Panalytical, UK) at the Department of Geology, University of Delhi. The XRD traces of the non-oriented powders of 24 samples were examined following Wilson (1987) for identification and to determine the various proportions of clay minerals (smectite (Sm): 14–15 Å;

kaolin: 7 Å; mica (M): 10 Å), non-clay mineral silicates (Q: 3.34 Å; feldspar (F): 3.2 Å), iron oxide minerals (hematite, Fe_2O_3: 2.69 Å; goethite, α-FeO(OH): 2.45 Å; ferrihydrite, $Fe_2O_3.0.5(H_2O)$: 2.56 Å; feroxyhyte, δ-FeO(OH): 1.67 Å; lepidocrocite, γ-FeO(OH): 3.29 Å; maghemite, γ-Fe_2O_3: 2.51 Å; magnetite, Fe_3O_4: 2.53 Å), Mn oxide minerals (2.02 Å) and gypsum ($CaSO_4.2H_2O$: 2.34 Å). The relative abundances of these minerals were determined by measuring peak areas or integrated intensities for each mineral, and the sum of peak areas of all identified minerals was taken as 100%. The total amount of iron oxide mineral phases in the XRD traces was compared with the total iron oxide determined using X-ray fluorescence (XRF) analysis, and only variations of <±5% were detected.

Clay mineralogical analysis

For clay mineralogy, the TC (<2 μm) and FC (<0.2 μm) fractions of the sediments were separated using the pipette method after the

removal of organic carbon, carbonate and free iron following the procedure of Jackson (1979). Orientated clay fractions of TC and FC were subjected to XRD analysis in the 3–30°2θ range using the abovementioned equipment at the University of Delhi. The clay fractions were saturated with Ca and solvated with ethylene glycol (Ca-Eg), and the K-saturated samples were heated to 25°C, 110°C, 330°C and 550°C. The identification of the clay minerals was done following Jackson (1979). The Sm is characterized by 14.0–15.0 Å (001) XRD peaks in Ca-saturation that increase to 17.0–19.0 Å upon solvation with ethylene glycol (Ca-Eg) at ambient temperature. Upon K-saturation and heating, the 001 peak of Sm shifts gradually to 12.0–13.0 Å at 25°C, 11.0–12.0 Å at 110°C, 10.5–11.5 at 330°C and finally to 10 Å (001) and 5 Å (002) at 550°C. The Ka is characterized by 7.20 Å (001) and 3.57 Å (002) peaks in Ca-saturation that are not affected either by solvation with ethylene glycol (Ca-Eg) at ambient temperature or by K-saturation and heating at 25°C, 110°C and 330°C, but they collapse at 550°C.

The interlayering in the 7.2 Å mineral phase was identified based on its slight shift and asymmetry towards low angles on glycolation and heating. Its broad basal reflections and absence of higher-order reflections were used to confirm kaolin (Wilson, 1987; Bhattacharyya *et al.*, 1993; Srivastava *et al.*, 1998). In the Sm component, Al-hydroxy interlayering in the Sm phase was identified based on the incomplete expansion of the 14–15 Å peaks upon glycolation and broadening of the low angle side of the 10 Å on K-saturation and heating to 550°C (Barnhisel & Bertsch, 1989; Bhattacharyya *et al.*, 1993; Dietel *et al.*, 2019). Transformation of Sm to Ka (Sm/Ka) in the TC and FC fractions was identified based on a low-angle plateau at ~7.2 Å in the Ca-saturated samples that shifts to 8.0 Å upon glycolation (Wilson & Cradwick, 1972; Pal *et al.*, 1989; Srivastava *et al.*, 1998). The dioctahedral or trioctahedral nature of the clay minerals was determined from 060 reflections of the randomly orientated samples (Jackson, 1979). The crystal orders of Sm and Ka were estimated based on the width of the first-order reflection and the presence or absence of higher-order XRD peaks (Wilson, 1987; Bhattacharyya *et al.*, 1993; Srivastava *et al.*, 1998). Semi-quantitative estimates of the clay minerals were based on the principle outlined by Gjems (1967) with some modifications; namely, the same background curve was used for both solvated and ignited samples (Kapoor, 1972). Accordingly, clay mineral percentages were calculated from Eg-solvated samples after measurement of the intensities of various reflections. The integrated intensities or areas of (001) peaks were measured for Sm (17 Å), Ka (7 Å), M (10 Å), Q (3.34 Å) and F (3.20 Å) and the sum of all these was taken as 100% to calculate the relative percentage of the various mineral phases.

Results

Bulk mineralogy

The bulk mineralogy determined by XRD of the randomly oriented powder samples of the 24 beds of the Giral mine section shows distinct variations in abundance of clay minerals (Sm, Ka, M), non-clay silicates (Q, F), iron oxides, Mn oxides and gypsum in each bed. The results of the bulk mineralogy are summarized in Figs 3–5 and Table 2. The bulk mineralogy of the 24 beds is characterized by varying proportions of clay minerals, non-clay silicates, iron oxides, Mn oxide and gypsum (Figs 3–5).

The clay beds consist on average of 59% clay minerals, 19% Q and F and 13% iron oxide minerals (Fig. 3 & Table 2). The silty clay beds consist on average of 43% clay minerals, 9.5% Q and F and 45% iron oxide minerals (Fig. 3 & Table 2). The silty loam beds consist on average of 28% clay minerals, 5% Q and F and 59% iron oxide minerals (Fig. 3 & Table 2). The sandy loam bed consists of 36% clay minerals, 10% Q and F and 46% iron oxide minerals (Fig. 3 & Table 2). Finally, the fine-grained sand beds consist on average of 17% clay minerals, 11% Q and F and 69% iron oxide minerals (Fig. 3 & Table 2).

The clay beds contain relatively low amounts of iron (13% average iron oxide minerals) in comparison to silty clay (45% average iron oxide minerals), silty loam (59% average iron oxide minerals), sandy loam (45.5% average iron oxide minerals) and fine-grained sands (69% average iron oxide minerals). The relative abundances of iron and manganese minerals in the 24 beds of the Giral mine follow the order hematite > goethite > ferrihydrite > feroxyhyte > lepidocrocite > magnetite > maghemite > Mn oxide (Table 2). Hematite varies from nil to 55%, goethite varies from nil to 34%, ferrihydrite varies from nil to 19%, feroxyhyte varies from nil to 11%, lepidocrocite varies from nil to 11.8%, maghemite varies from nil to 6.8%, magnetite varies from nil to 13.9% and the Mn oxide minerals vary from nil to 2.9% (Table 2).

Total clay (<2 μm) mineralogy

The mineralogy of the TC fraction (<2 μm) determined from orientated mounts is dominated by Sm and Ka, whereas M, Q and F occur in minor or trace amounts. The TC fraction mineralogy of the representative samples from 24 beds of the Giral mine section is summarized in Figs 6–8 and Table 3 and is briefly described here.

A semi-quantitative estimate of the XRD peaks shows that Sm is the main phase in all 24 beds and varies between 54 and 89% at various levels of the section (Fig. 6 & Table 3). Sm is marked by distinct trends of abrupt decrease from 81 to 60% between 23 and 20 m depth, followed by an increase from 63 to 82% between 20 and 9.5 m depth, then again it displays an abrupt decrease from 76 to 55% between 9.5 and 5.7 m depth, and then a further increase up to 89% with minor changes at the top of the section (Fig. 6 & Table 3). The Sm in most of the samples also showed Al-hydroxy interlayering and Sm/Ka interstratification in varying amounts at various levels of the section (Table 3).

Ka also occurs in all 24 beds and varies between 6 and 38% at various levels of the section (Fig. 6 & Table 3). Similarly to Sm, the Ka is also marked by distinct trends of abrupt increase or decrease, and it is anti-correlated with the Sm abundance (Fig. 9). Ka increases abruptly from 8% to 25% at 21 m depth. The increased abundance of the Ka continues from 21 to 5.5 m depth of the section, with several spikes of 25% at 21 m depth, 25% at 10 m depth, 35% at 8.5 m depth and 38% at 5.5 m depth with intervening low contents (5–8%; Fig. 6). In addition to Sm and Ka, the M, F and Q with their characteristic peaks occur in minor or trace amounts (Table 3).

Fine clay (<0.2 μm) mineralogy

The mineralogy of the FC fraction (<0.2 μm) of the 24 beds of the Giral mine section is summarized in Figs 6–8 and Table 4 and is briefly described here. Similarly to the TC fraction, the FC fraction is also marked by the dominance of Sm and Ka, with distinct trends of increases and decreases in the 32 m section (Figs 6–8 & Table 4). In the FC fraction of all 24 beds, the Sm varies between 66 and 92% at various levels (Table 4). The Sm is abundant (90–
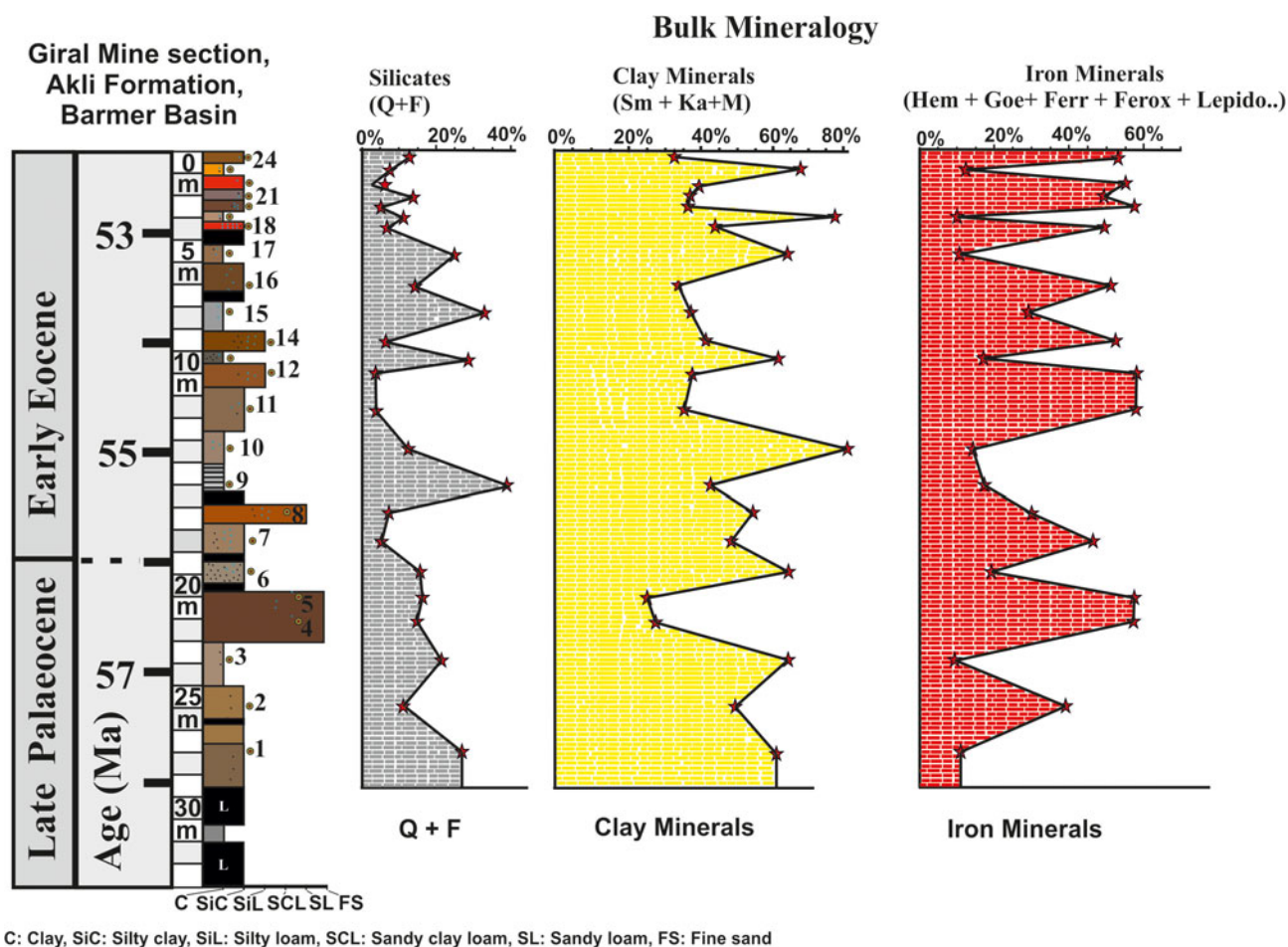
Figure 3. Bulk mineralogy of the 24 beds based on XRD of the randomly oriented powder samples showing the depth-wise distribution of the iron oxide minerals, clay minerals and non-clay silicates. Semi-quantitative estimates of the clay minerals (Sm, Ka, M), non-clay minerals (Q, F) and iron oxide minerals (hematite, goethite, ferrihydrite, feroxyhyte, lepidocrocite, maghemite, magnetite), Mn oxide (Mn_3O_4) and gypsum are summarized in Table 2.

92%) in the lower part (22–27 m depth) and in the upper part (1–3 m depth) of the section (Table 4). Sm shows an abrupt decrease from ~90 to 67% at 20 m depth, which continues with minor changes up to 10 m depth (Fig. 6 & Table 4). The hydroxy interlayering in Sm is more widespread in the FC fraction. It varies from nil to 20% at various levels (Table 4). The interstratified Sm/Ka phase is an intermediate phase of the transformation of Sm into Ka and is also more abundant in the FC fraction compared to the TC fraction (Table 4).

The Ka in the FC fraction occurs in all 24 samples, varying between 6 and 30% and showing abrupt to gradual changes in abundance (Table 3). Similarly to the TC fraction, the Ka in the FC fraction also shows strong anti-correlation with Sm (Fig. 9). The increase in Ka content in the FC fraction is marked by several spikes of 25% at 20–21 m depth, 26% at 10–11 m depth, 25–27% at 9 m depth and 30% at 5.5 m depth (Fig. 6 & Table 4). In addition, similarly to the TC fraction, the 7.2 Å peak of Ka in FC fraction is also marked by increased intensity and broadening during K-saturation and heating (Figs 7 & 8). The transformation of Sm into Ka in the FC fraction is much more distinct and frequent than in the TC fraction (Table 4). In addition to Sm and Ka, M, F and Q also occur in minor or trace amounts (Table 4).

The clay mineralogy of the TC and FC fractions of the 32 m Giral mine sections shows an abrupt increase in the abundance of Ka at 20–22, 10–11, 5–6 and 2–3 m depths, with corresponding decreases in abundance of Sm related to the various age intervals of the Akli Formation (Fig. 6). The age estimate of the 32 m Giral mine section shows that the varying abundances in the clay mineralogy at these depth intervals of the section correspond to: (1) pre-P–E transition (i.e. bed nos. 3 and 4), (2) during the P–E transition (i.e. bed nos. 5–8) and (3) post-P–E transition (i.e. bed nos. 12–14 and 18–20). The uppermost 2 m of the section with very high Sm (85–90%) and low Ka contents (5–11%) are similar to the lower part (25–27 m) of the section, showing high Sm (81–92%) and low Ka contents (5–10%) that characterize the pre-P–E and post-P–E clay mineralogies.

Discussion

Clay minerals in Akli Formation sediments and implications for hyperthermals in the palaeotropics

The PETM and subsequent hyperthermals have been studied extensively based on various proxies mainly in mid- to high-
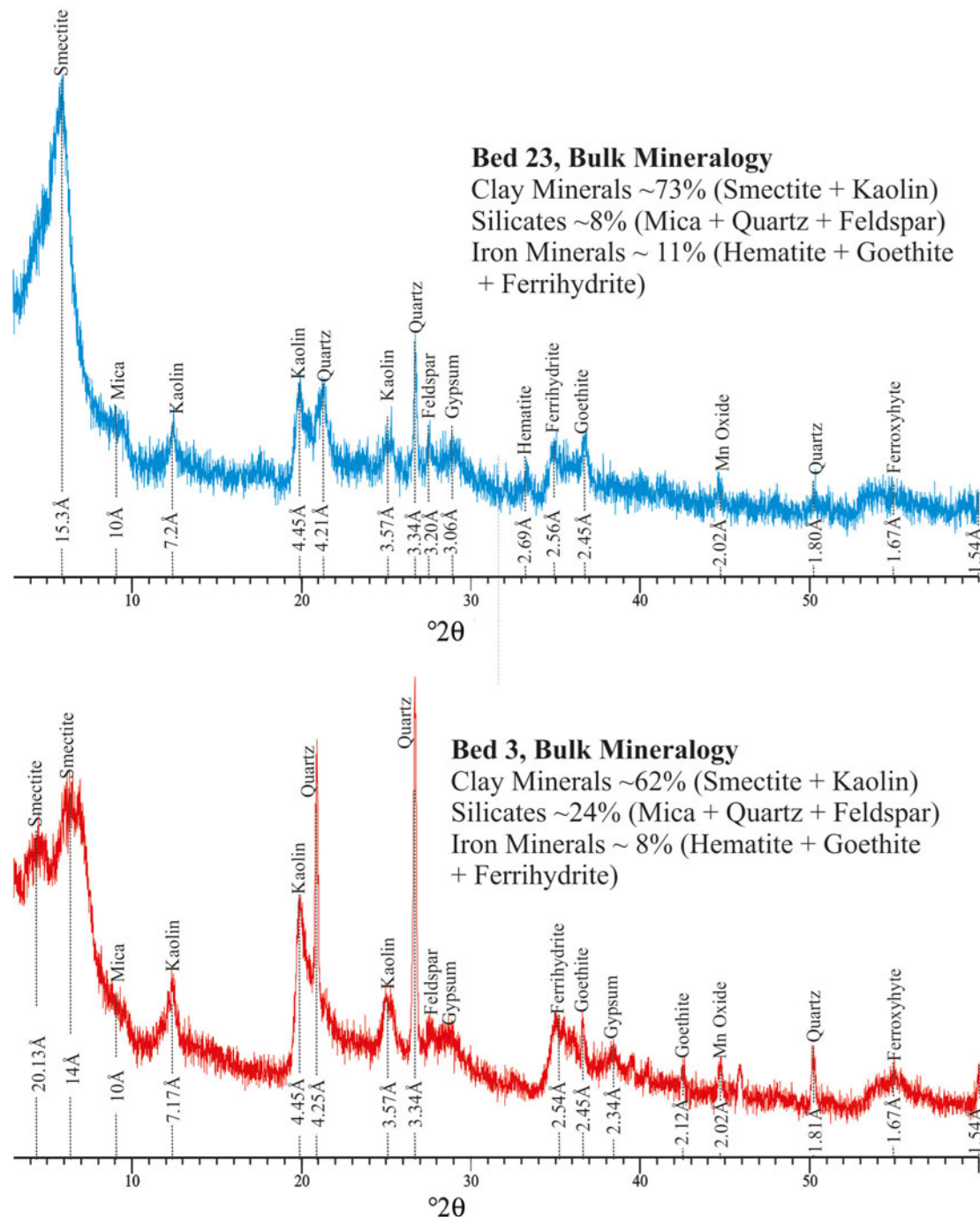
Figure 4. XRD traces of random powder samples of beds 23 and 3. These beds are dominated by clay minerals (62–73%) and small amounts of iron oxide minerals (8–11%).

latitude regions (Kennet & Scott, 1991; Zachos *et al.*, 2003; Wing *et al.*, 2005; Pagani *et al.*, 2006; Westerhold *et al.*, 2009; Zeebe *et al.*, 2009). The clay mineral assemblage and in particular the increased abundance of kaolin has been considered to be one of the potential proxies reflecting hyperthermals in many mid- to high-latitude regions (Gibson *et al.*, 1993, 2000; Clechenko *et al.*, 2007; Kemp *et al.*, 2016; Tateo, 2020). However, the tropical environmental conditions during the PETM are not well understood, and there is a large uncertainty about the tropical ecosystem during the PETM at the global level (Jaramillo *et al.*, 2010;

Walters *et al.*, 2022). The present study reports the first clay mineral evidence of the PETM and ETM2 hyperthermals from a near-equatorial region represented by the Giral mine section of the Akli Formation. The palaeogeographical reconstruction of the Akli Formation, Barmer Basin, shows that it was located at 4.5° S in the near-equatorial region during the P–E transition (Fig. 10; after Scotese, 2010). Thus, the 32 m section of the Giral mine of the Akli Formation provides an important archive of the P–E transition sediments that could be used to explore the PETM and the subsequent hyperthermals in the palaeotropics.
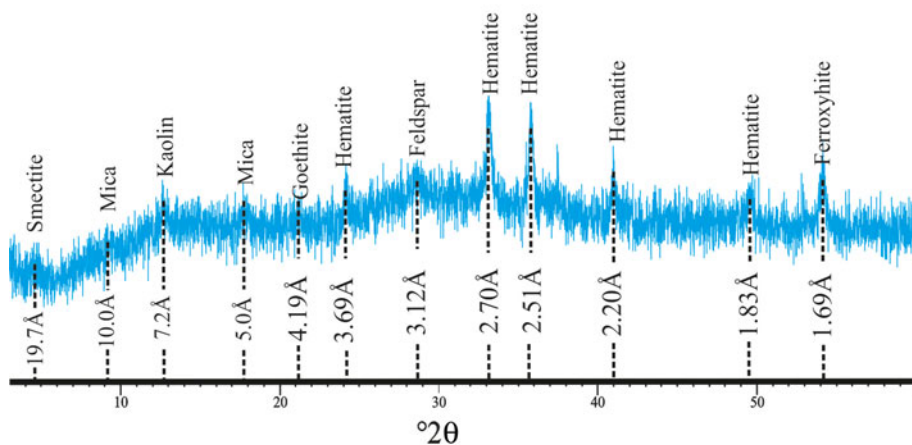
Bed 16, Bulk Mineralogy
Clay Minerals ~28% (Smectite + Kaolin)
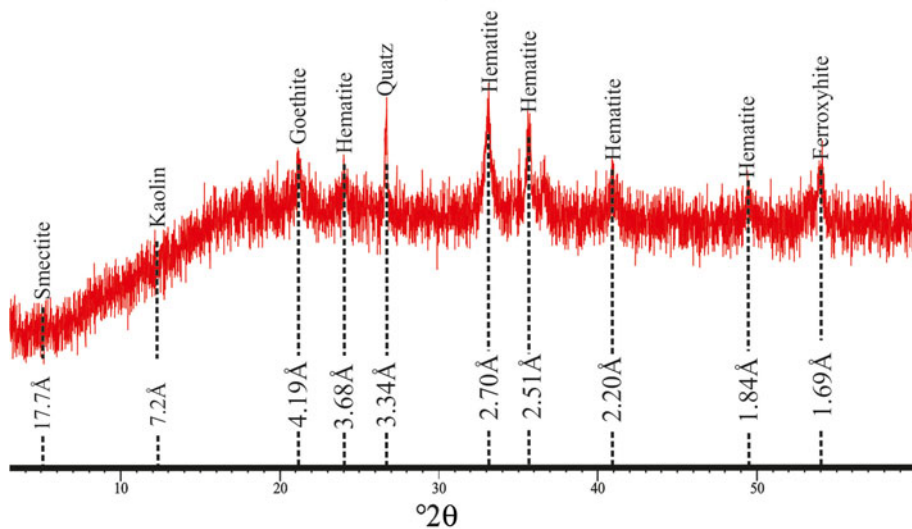Silicates ~20% (Mica + Quartz + Feldspar)
Iron Minerals ~ 51% (Hematite + Goethite + Ferroxyhite)

Bed 4, Bulk Mineralogy
Clay Minerals ~18% (Smectite + Kaolin)
Silicates ~11% (Mica + Quartz + Feldspar)
Iron Minerals ~ 70% (Hematite + Goethite + Ferroxyhite)

Figure 5. XRD traces of random powder samples of bed 4 and bed 16. These beds are dominated by iron oxide minerals (51–71%) and lesser amounts of clay minerals (18–28%).

The clay mineral record of both the TC (<2 μm) and FC (<0.2 μm) fractions of the Akli Formation is characterized by the dominance of Sm (60–92%) and Ka (5–38%). Unlike the modern sediments of the near-equatorial region, which consist mainly of Ka, the Akli Formation consists of mainly Sm and Ka because it originates from weathering of F-rich igneous rocks under tropical conditions. The Sm is montmorillonite with high Al and Fe contents. The 060 reflections of the TC and FC fractions at ~1.50 Å confirmed that Sm is dioctahedral. The chemical formula of the montmorillonite is $((Si_{3.52}Al_{0.48})Al_{1.48}Fe_{0.39}Mg_{0.13})O_{10}(OH)_2)M_{+0.62}$ (Grim & Güven, 1978).

The studied section shows abrupt changes in the abundances of Sm and Ka and the Ka:Sm ratio in pre-P–E transition, during P–E transition and post-P–E transition sediments that are related to palaeoenvironmental changes and weathering conditions in the palaeotropics (see Fig. 6 & Tables 3 & 4). The clay mineralogy of the Akli Formation suggests a 3–4-fold increase in Ka during the P–E transition in comparison to pre-P–E transition and post-P–E transition sediments (Fig. 6 & Tables 3 & 4). The 3–4-fold increase in Ka and the Ka:Sm ratio in the P–E transition sediments of the Akli Formation is attributed to increased warming and precipitation, which caused a further increase in the intensity of chemical weathering in the tropics. The increased chemical

Table 2. Bulk mineralogy based on random powder XRD of the 24 beds of the Giral mine section of the Akli Formation.

Sample/ bed no.	Depth (m)	Clay minerals			Other silicate minerals		Iron minerals								Total iron oxide minerals (%)	Gypsum/ anhydrite (%)
		Sm (%)	Ka (%)	M (%)	Q (%)	F (%)	Hem	Goe	Ferri	Ferrox	Lepid	Mghm	Mgm	Mn oxide		
24	0.15	17.6	10.7	5.1	5.1	7.7	43.2	–	10.5	–	–	–	–	–	53.7	–
23	0.65	61.4	16.2	–	4.6	3.2	2.1	3.6	5.8	–	–	–	–	1.0	11.5	3.3
22	1.10	29.5	10.1	–	1.7	–	42.5	4.2	–	9.8	–	–	–	–	56.5	–
21	1.60	21.8	14.8	–	7.9	6.6	32.9	5.7	–	–	–	–	10.2	–	48.8	–
20	2.10	27.2	6.6	2.7	–	5.3	45.9	–	–	–	11.8	–	–	–	57.7	–
19	2.75	59.6	19.1	–	4.9	5.7	–	–	–	8.6	–	–	–	1.6	8.6	–
18	3.25	28.3	7.7	8.0	3.5	3.0	33.7	–	2.3	7.0	6.4	–	–	–	49.4	–
17	4.40	40.3	12.2	12.2	16.5	8.4	–	2.1	2.8	3.5	–	–	–	1.8	8.4	–
16	5.75	17.2	10.4	5.6	–	14.5	40.3	–	–	10.8	–	–	–	–	51.1	–
15	7.50	25.9	2.5	8.3	25.6	7.5	16.8	8.8	3.8	–	–	–	–	–	29.4	–
14	8.50	11.9	8.8	20.3	7.5	2.8	4.2	34.2	4.4	–	5.3	–	–	–	48.1	–
13	9.30	27.3	17.4	9.9	16.7	11.6	–	3.0	10.5	–	–	1.3	–	1.7	14.8	–
12	10.10	14.6	5.7	6.5	–	–	8.1	33.7	19.4	–	11.5	–	–	–	72.7	–
11	11.75	22.5	8.5	–	3.9	–	11.8	33.8	5.5	–	–	–	13.9	–	65.0	–
10	13.25	62.6	18.1	–	11.3	1.4	–	1.1	–	–	–	3.2	–	–	4.3	3.4
9	15.00	19.1	5.3	18.2	10.2	29.0	–	9.6	7.7	–	–	–	–	1.4	17.3	–
8	16.00	18.1	18.6	–	10.0	–	8.4	21.2	5.7	–	–	10.2	–	4.3	45.5	–
7	17.50	26.8	9.2	11.8	5.2	–	33.3	3.9	–	8.3	–	–	–	–	45.5	–
6	19.00	35.9	28.8	–	12.3	3.0	–	–	8.4	11.0	–	–	–	–	19.4	–
5	20.00	10.5	8.5	–	10.2	2.2	53.5	14.5	–	–	–	–	–	–	68.0	–
4	21.00	8.5	8.8	–	9.0	1.5	55.2	15.9	–	–	–	–	–	–	71.1	–
3	23.00	43.6	18.3	2.8	21.2	–	–	2.8	–	5.6	–	–	–	1.1	8.4	3.0
2	25.00	31.6	8.6	9.5	7.5	3.5	19.7	–	6.0	–	8.6	4.8	–	–	39.1	–
1	27.00	52.3	5.6	2.8	11.6	14.8	1.7	–	7.6	–	–	–	1.7	–	11.0	2.2

Hem = hematite (Fe_2O_3); Goe = goethite (α-FeO(OH)); Ferri = ferrihydrite ($Fe_2O_3.0.5(H_2O)$); Ferrox = feroxyhyte (δ-FeO(OH)); Lepido = lepidocrocite (γ-FeO(OH)); Mghm = maghemite (Fe_2O_3, γ-Fe_2O_3); Mgm = magnetite (Fe_3O_4), Mn oxide = Mn_3O_4.
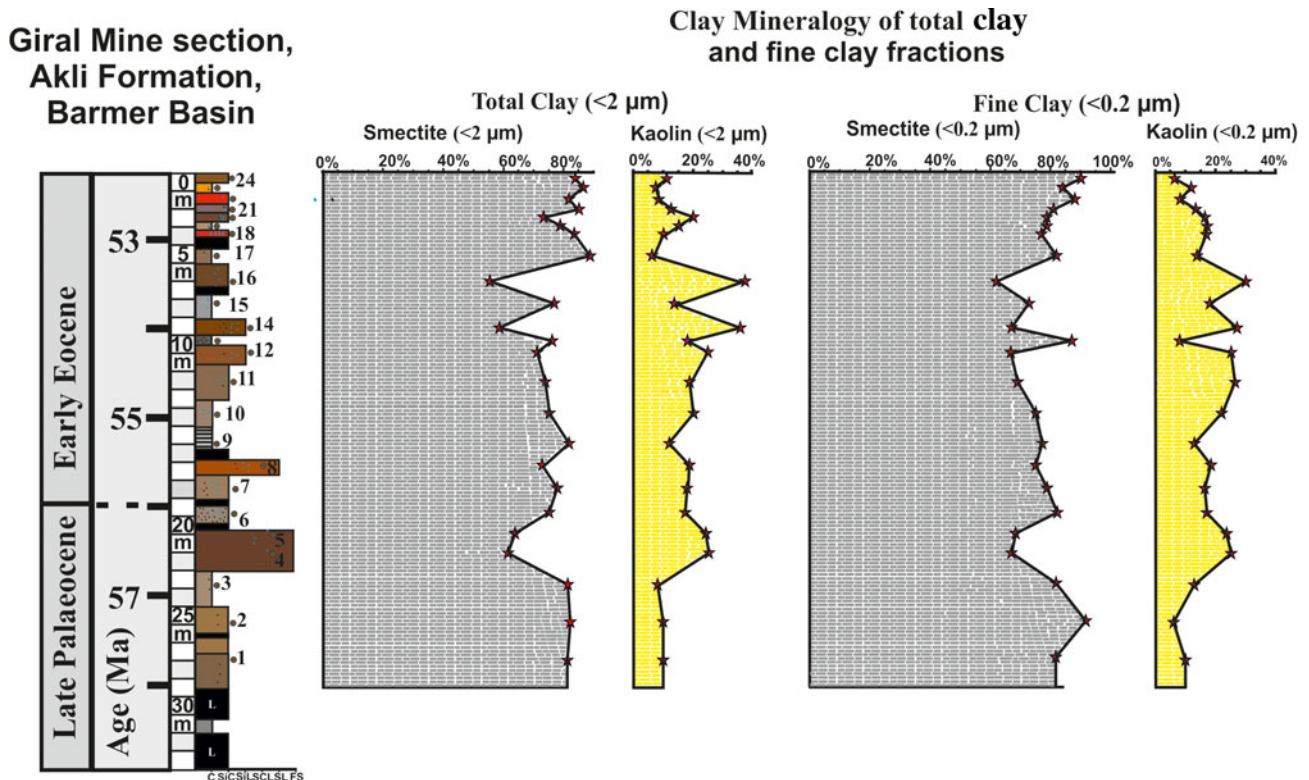

Figure 6. Depth-wise distribution of Sm and Ka in the TC (<2 μm) and FC (<0.2 μm) fractions of the 24 beds, showing abrupt increases and decreases in Ka and Sm in sediments of the Giral mine section.
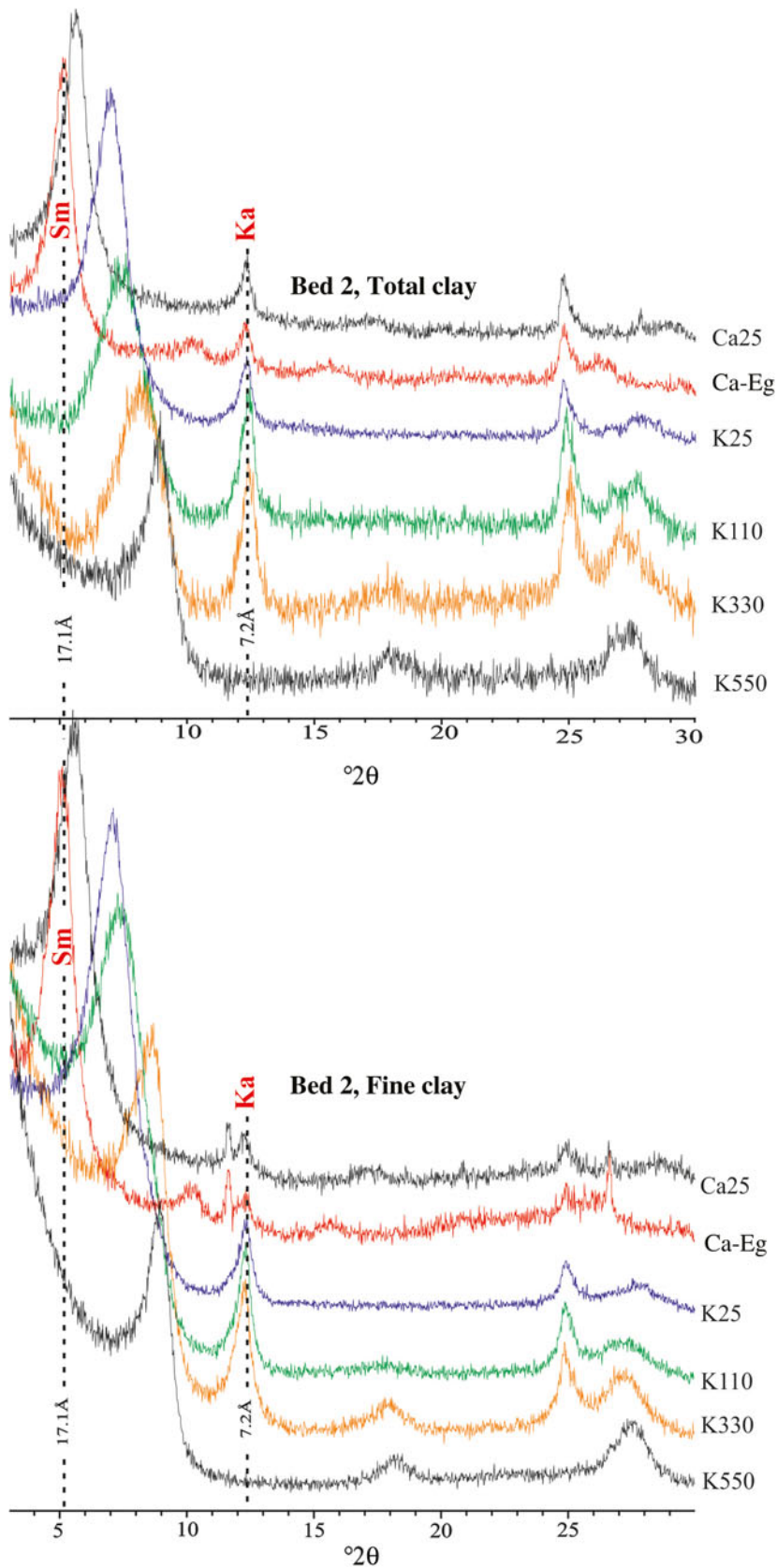
Figure 7. Bed 2 XRD traces of the TC (<2 μm) and FC (<0.2 μm) fractions under various auxiliary treatments: Ca-saturation and solvation with ethylene glycol (Ca-Eg) and K-saturation and heating at 25°C, 110°C, 330°C and 550°C.

weathering during the P–E transition is suggested by the following key features: (1) the abrupt decrease in the Sm content from 90% to 60% during the P–E transition in comparison to pre-P–E and post-P–E sediments; (2) the grain-size change from silty clay or clay to loam and fine-sand during the P–E transition due to increased runoff; (3) the increased sequestration of iron oxides
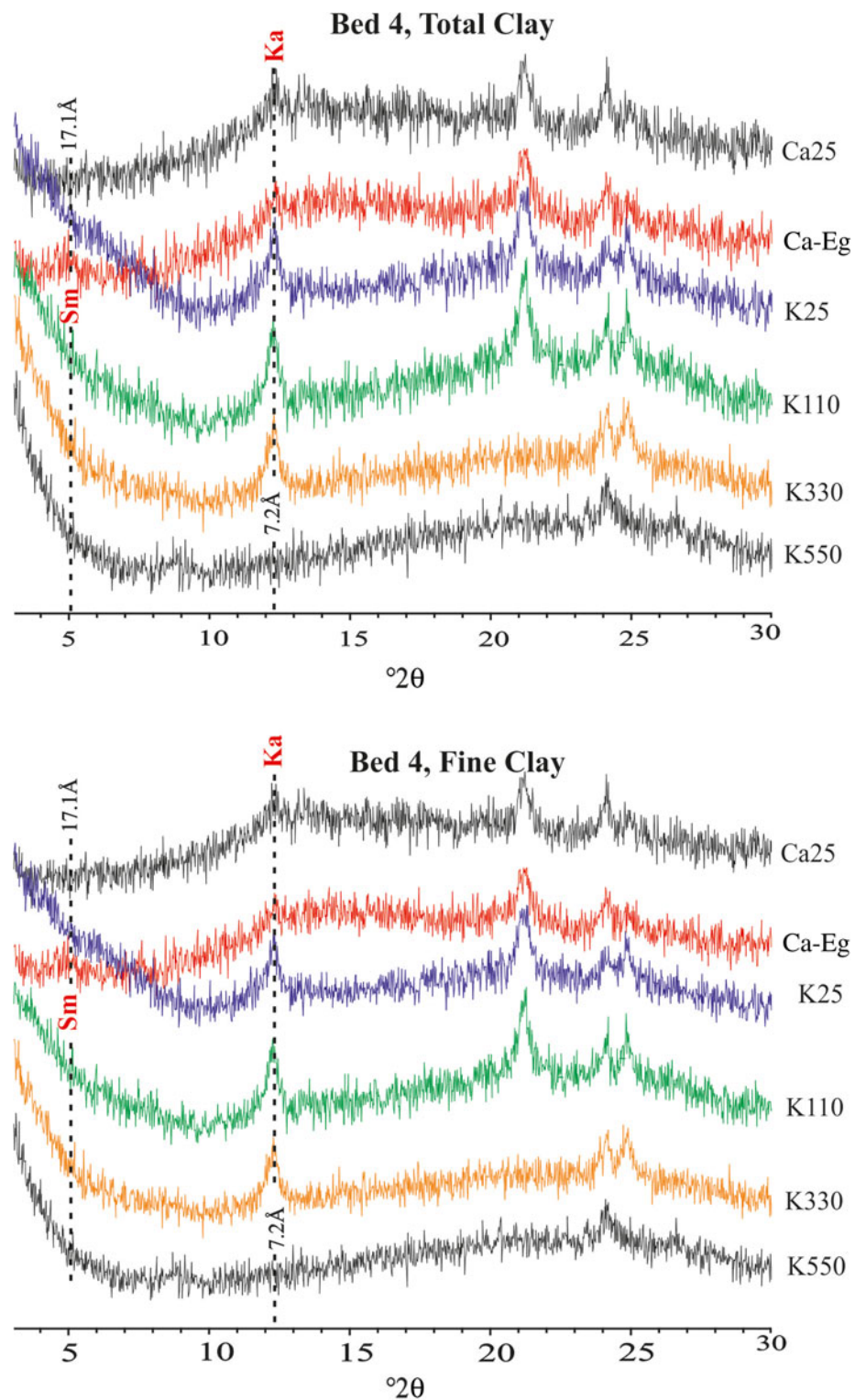
Figure 8. Bed 4 XRD traces of the TC (<2 μm) and FC (<0.2 μm) fractions under various auxiliary treatments: Ca-saturation and solvation with ethylene glycol (Ca-Eg) and K-saturation and heating at 25°C, 110°C, 330°C and 550°C.

in sediments, which is more evident when goethite (α-FeO(OH)) is correlated with Ka (Fig. 9); (4) the abrupt occurrence of ~20% charcoal fragments in sediments at the P–E boundary (Fig. 11); (5) the abrupt appearance and increased proportion of gypsum to ~8–10%; and (6) the acidic conditions (pH 4–5) during the P–E transition in comparison to neutral pH conditions found for the pre-P–E and post-P–E sediments of the Akli Formation (Fig. 11).

The abovementioned observations regarding clay minerals, iron oxide minerals, charcoal, gypsum and acidic conditions indicate further warming and wetting in the normal tropical conditions resulted in further increases to chemical weathering linked to the PETM and ETM2 hyperthermals. The clay mineralogy of the Akli Formation P–E transition sediments, showing warming, wetting and increased chemical weathering, is also well-supported by the carbon isotopic composition (δ13C) of the sediments of the

Table 3. TC fraction (<2.0 µm) mineralogy of the 24 beds in the Giral mine sediments of the Akli Formation. Mineral abbreviations follow Table 2.

Sample/bed no.	Depth (m)	Sm (%)	Ka (%)	M (%)	Q (%)	F (%)	Sm: hydroxy interlayering (%)	Sm/Ka[a]
24	0.15	83.6	11.4	T	1.6	3.2	16–20	a
23	0.65	86.6	7.2	–	2.7	3.3	5–10	a
22	1.10	82.4	8.2	T	3.9	5.2	5–10	a
21	1.60	84.7	11.5	T	1.4	2.4	5–10	a
20	2.10	73.4	19.7	T	2.7	4.0	16–20	a
19	2.75	79.4	14.9	T	3.5	2.1	16–20	b
18	3.25	84.3	9.8	T	2.4	3.3	5–10	a
17	4.40	89.2	5.5	T	2.2	2.9	5–10	a
16	5.75	54.5	37.8	T	3.7	3.7	20–25	b
15	7.50	77.3	14.3	0.8	3.4	4.0	16–20	a
14	8.50	57.5	34.7	T	2.8	4.7	20–25	b
13	9.30	75.6	18.1	T	3.3	2.9	5–10	a
12	10.10	71.2	25.0	T	1.9	1.9	16–20	b
11	11.75	73.8	18.9	0.7	2.6	3.9	5–10	a
10	13.25	75.1	19.5	T	2.6	2.0	16–20	b
9	15.00	82.4	11.8	T	1.7	4.5	5–10	a
8	16.00	73.3	19.4	T	2.1	5.2	16–20	a
7	17.50	77.9	17.8	0.9	1.3	1.9	16–20	a
6	19.00	74.6	16.8	1.4	4.1	2.9	5–10	a
5	20.00	63.5	24.6	–	5.5	5.9	16–20	b
4	21.00	61.2	25.2	–	5.4	5.7	16–20	b
3	23.00	81.1	8.4	T	3.6	6.8	5–10	b
2	25.00	82.2	9.9	T	3.1	4.7	5–10	a
1	27.00	81.3	10.4	T	3.7	4.4	5–10	a

[a]Sm/Ka = transformation of Sm into Ka: a = <10%; b = >10%.
T = trace.

studied section and the nearby lignite mines of western India (Khozyem *et al.*, 2021). The Akli Formation sediments are marked by the two prominent CIEs linked to the PETM and subsequent ETM2 hyperthermals (Khozyem *et al.*, 2021). The first 2–3‰ negative shift of $\delta^{13}C_{org}$ reported by Khozyem *et al.* (2021), with a corresponding 3–4-fold increase in the Ka at ~20 m depth in the Akli Formation, is consistent with the PETM, whereas the second 2–3‰ negative shift of $\delta^{13}C_{org}$ corresponds to another 3–4-fold increase of Ka in the upper part of the 32 m section, which is related to the ETM2 (Fig. 11). The warming and wetting interpreted here based on clay mineralogy are consistent with globally recorded warming, CIEs, acidification and an abrupt change in the hydrological cycle (Dickens *et al.*, 1995; Zachos *et al.*, 2005; McInerney & Wing, 2011; Westerhold *et al.*, 2020). The palynological work on the Akli Formation sediments also supports this interpretation through the appearance of *Nypa*-like pollens during the P–E transition, a marker of warm, tropical regions (Chaloner, 1968; Morley, 2000; Tripathi *et al.*, 2003, 2009).

Equatorial Ka pulse during P–E hyperthermals in relation to mid- to high latitudes

The Ka pulse (3–4-fold increase) in sediments deposited during the PETM has been used as an important criterion defining intense chemical weathering due to enhanced warming and significant precipitation during the hyperthermals (Gibson *et al.*, 1993; Robert & Kennett, 1994, 1997; Knox, 1996; Gawenda *et al.*, 1999; Bolle & Adatte, 2001; Kemp *et al.*, 2016). However, most of the examples reporting a Ka pulse during the PETM are from mid- to high latitudes, except for one from low latitudes (Bolle & Adatte, 2001). The mid- and high-latitude examples of the Ka pulse (Fig. 12) include: (1) the New Jersey Formation

from north Atlantic coastal plains showing an increase in Ka from 4–8% to 38–58% during the PETM (Gibson *et al.*, 1993); (2) the latest Palaeocene sediment core from eastern Antarctica showing an increase of Ka in sediments from ~5% to ~30% during the PETM due to increased chemical weathering, temperature rises and increased precipitation (Robert & Kennett, 1994); (3) the P–E boundary events from north-west Europe and the North Sea showing an appreciable increase in the proportion of Ka (Knox, 1996; Kemp *et al.*, 2016); and (4) the P–E Zumaria Series of northern Spain showing a large increase in the Ka:Sm ratio during the PETM (Gawenda *et al.*, 1999). Apart from mid- to high-latitude Ka pulses reported worldwide, the P–E transition sediments from the Tethys Sea at ~24° N palaeolatitude also show an appreciable increase of Ka due to increased chemical weathering (Fig. 12; Bolle & Adatte, 2001). The Ka pulse recorded in the Akli Formation representing a near-equatorial palaeogeographical location confirms increased chemical weathering in the tropical regions during the P–E transition. Thus, the PETM and the subsequent hyperthermals occurred globally and influenced both low and mid- to high latitudes in similar ways (Carmichael *et al.*, 2017; Walters *et al.*, 2022).

Genesis of Sm and Ka during P–E hyperthermals in the palaeotropics

To trace the origin of Sm and its transformation, we refer to the weathering of F-rich source rocks under humid, tropical conditions. Indeed, the formation of Sm and Ka in tropical environments is attributed to the hydrolysis of silicate minerals such as F and M during weathering (De Kimpe *et al.*, 1961; Rengasamy *et al.*, 1978; Gilkes & Suddhiprakran, 1979; Anand *et al.*, 1985). Sediments of the Akli Formation were sourced mainly from the Malani Igneous Suite, consisting of rhyolite, tuff and granite (Eby & Kochhar, 1990; Maheshwari *et al.*, 2001; Gregory *et al.*, 2009). The palaeolatitudinal history of the Akli Formation shows that it was located at ~4.5° S in a near-equatorial position (Fig. 10). The expected temperature and precipitation anomalies over equatorial or tropical regions during the PETM indicate an increase in average temperature of ~3–5°C and a 25–50% increase in precipitation (Inglis *et al.*, 2020; Rush *et al.*, 2021). The present-day climate in the equatorial region is marked by an 28°C average temperature, 2100 mm average precipitation and very high humidity (Meng *et al.*, 2016; Kristo *et al.*, 2017). Thus, increases in temperature and rainfall during the P–E transition in the near-equatorial region must have intensified the chemical weathering that caused a 3–4-fold increase in Ka at the expense of Sm in the Akli Formation (Fig. 11).

The increased amounts of Ka at the expense of Sm can be understood by the weathering characteristics of the F-rich igneous rocks that indicate Sm as the first weathering product under humid conditions (Tardy *et al.*, 1973). This is in accordance with the studies of <2 µm fractions separated from weathering rinds of the basalts from central and southern India, which showed a dominance of dioctahedral Sm and very small amounts of Ka (Pal & Deshpande, 1987). The presence of Ka next to excess Sm in the weathering rinds has been explained due to there being larger pores in the mineral grains (Tardy *et al.*, 1973; Pal & Deshpande, 1987). This is also consistent with the weathering profiles of the alkali igneous rocks such as rhyolite and granite showing the dominance of Sm and a small proportion of Ka in the clay fractions due to hydrolysis of F (Harriss & Adams, 1966; Nesbitt & Young, 1984). The great amounts of Sm after
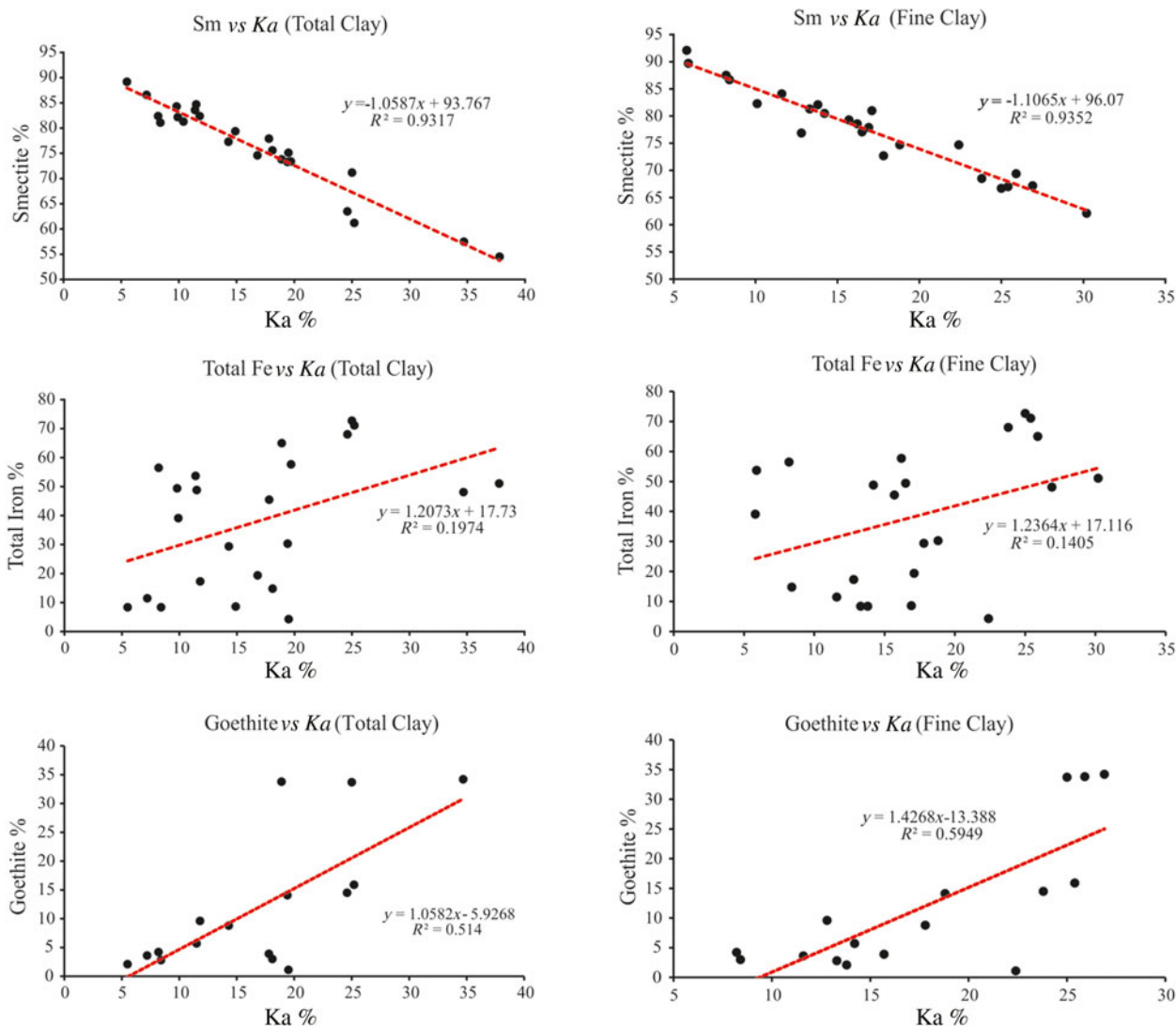
Figure 9. Correlation of Sm *vs* Ka, total iron *vs* Ka and goethite *vs* Ka in the TC (<2 μm) and FC (<0.2 μm) fractions of the 24 beds.

weathering of alkali extrusive rocks can be explained by the weathering kinetics of alkali volcanics and their crystalline equivalents (Nesbitt & Young, 1984). Glass with an albite and K-feldspar composition is much less stable than its crystalline equivalents under ambient weathering conditions (Nesbitt & Young, 1984). Under such conditions, when volcanic glass is the primary phase that undergoes weathering, the stability field of Sm is expanded greatly, which results in a larger amount of Sm as the weathering product than in the crystalline phase (White *et al.*, 1963; Nesbitt, 1977; Nesbitt & Young, 1984). Hence, the large amounts of Sm (80–90%) and small amounts of Ka (5–10%) in the pre-PETM and post-PETM sediments of the Akli Formation are due to the weathering of rhyolite and granite under humid, tropical conditions (Figs 6 & 11).

The increased proportion of Ka (25–30%) during the PETM and subsequent ETM2 in sediments of the Akli Formation is attributed to warming by 3–5°C and to precipitation increasing by 25–50% in the equatorial region. This change of climate to much warmer and wetter conditions during the PETM than during the pre-PETM period resulted in more intense chemical

weathering and hydrolysis of F in the rhyolite source of the Akli Formation sediments. This is also supported by increased acidic conditions (pH from 7.5 to 4 and 5), decreased Sm proportions from 85–90% to 55–60%, increased proportions of iron oxide minerals with a larger amount of goethite and unusual appearances of charcoal at ∼20% in sediments deposited during the PETM (Fig. 11). In such acid-weathering environmental condition, Sm is highly unstable and transforms into 1:1 clay minerals, such as Ka (Herbillon *et al.*, 1981; Chitale & Gueven, 1989; Bhattacharyya *et al.*, 1993). The possible mechanism that explains the conversion of the 2:1 layer silicate to a 1:1 structure involves hydroxy interlayering in Sm, interstratification between Sm and Ka and direct conversion of Sm into Ka (Herbillon *et al.*, 1981; Chitale & Gueven, 1989; Bhattacharyya *et al.*, 1993). This work on the clay mineralogy of the Akli Formation shows that Sm, in general, is characterized by Al-hydroxy interlayering, as the XRD traces of the TC and FC fractions are marked by an incomplete expansion of the 14–15 Å peaks on glycolation and broadening of the low-angle side of the 10 Å on K-saturation and heating to 550°C (Fig. 7). The hydroxy interlaying in Sm is

Table 4. FC fraction (<0.2 μm) mineralogy of the 24 beds in the Giral mine sediments of the Akli Formation. Mineral abbreviations follow Table 2.

Sample/ bed no.	Depth (m)	Sm (%)	Ka (%)	M (%)	Q (%)	F (%)	Hydroxy interlayering (%)	Sm/ Ka[a]
24	0.15	89.7	5.9	–	1.4	2.8	16–20	a
23	0.65	84.1	11.6	–	1.8	2.4	5–10	a
22	1.10	87.5	8.2	–	3.0	2.0	16–20	a
21	1.60	80.5	14.2	–	2.3	2.9	5–10	a
20	2.10	78.6	16.2	–	1.7	3.4	20–25	a
19	2.75	77.9	16.9	–	2.2	2.9	16–20	b
18	3.25	77.1	16.5	–	2.7	3.6	5–10	a
17	4.40	82.1	13.8	–	1.6	2.4	5–10	b
16	5.75	62.1	30.2	–	3.8	3.8	16–20	a
15	7.50	72.7	17.8	1.2	3.4	4.8	5–10	a
14	8.50	67.2	26.9	–	2.9	2.9	5–10	a
13	9.30	86.7	8.4	–	1.9	2.9	5–10	a
12	10.10	66.7	25.0	T	4.1	4.1	5–10	a
11	11.75	69.4	25.9	T	1.6	3.0	5–10	a
10	13.25	74.7	22.4	T	1.4	1.4	5–10	a
9	15.00	76.9	12.8	T	4.3	5.8	5–10	b
8	16.00	74.7	18.8	T	2.6	6.1	16–20	b
7	17.50	79.3	15.7	–	2.1	4.2	5–10	a
6	19.00	81.0	17.1	–	1.2	0.6	5–10	a
5	20.00	68.5	23.8	–	4.8	2.8	20–25	b
4	21.00	67.0	25.4	–	5.0	2.5	20–25	b
3	23.00	81.3	13.3	T	3.1	2.2	20–25	b
2	25.00	92.1	5.8	T	1.5	0.6	16–20	a
1	27.00	82.3	10.1	T	3.4	4.1	16–20	a

[a]Sm/Ka = transformation of Sm into Ka: a = <10%; b = >10%.
T = trace.

more pronounced in sediments of the Akli Formation deposited during the PETM and subsequent hyperthermals than before or after the PETM. The hydroxy interlayering in Sm is the result of an acid-weathering environment that causes the incorporation of hydroxy-Al polymeric components within the interlayer spaces of the expansible layer silicates (Barnhisel & Bertsch, 1989; Bhattacharyya et al., 1993; Dietel et al., 2019).

The Sm to Ka transformation is also a common feature of the Akli Formation sediments, which is increased during the PETM and subsequent hyperthermals (Table 3). The Sm to Ka transformation in the TC and FC fractions is indicated by a low-angle plateau at ~7.0 Å in the Ca-saturated samples that shifts to 8.0 Å upon glycolation (Figs 7 & 8). Interstratified Sm/Ka has been reported from the ferruginous soils of southern India and the well-developed soils of the Gangetic Plains due to increased humidity (Pal et al., 1989; Bhattacharyya et al., 1993; Srivastava et al., 1998), as well as elsewhere (Wilson & Cradwick, 1972; Norrish & Pickering, 1983; Delvaux et al., 1990). Because of these considerations, it is suggested here that the PETM and subsequent hyperthermal ETM2 events in the near-equatorial regions resulted in the large-scale transformation of Sm into 1:1 layer silicates through the following pathway:

Sm (after rhyolite weathering) → hydroxy interlayering (acid-weathering environment) → mixed-layer Sm/Ka (Sm to Ka transformation under a continued acid-weathering environment) → Ka
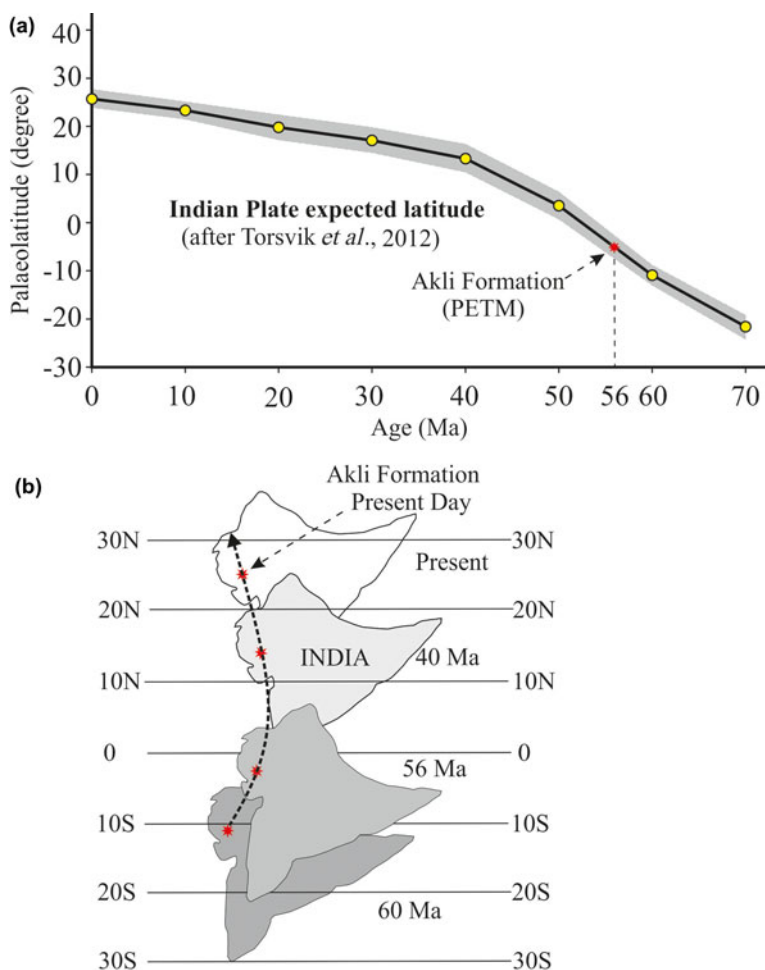

Figure 10. (a) Palaeolatitudinal position for the present-day location of Giral lignite mine (26.0502777, 71.2669444) on the Indian Plate (501) (www.paleolatitude.org, version 2.1; after Torsvik et al., 2012) calculated using the global apparent polar wander path where lower and upper bounds (grey) represent the 95% confidence interval. (b) A correlation of the equatorial climatic conditions of the Giral lignite mine with the palaeolatitudinal reconstruction of the Indian Plate at 60 Ma, 56 Ma (during the PETM), 40 Ma and in the present day (after Torsvik et al., 2012).
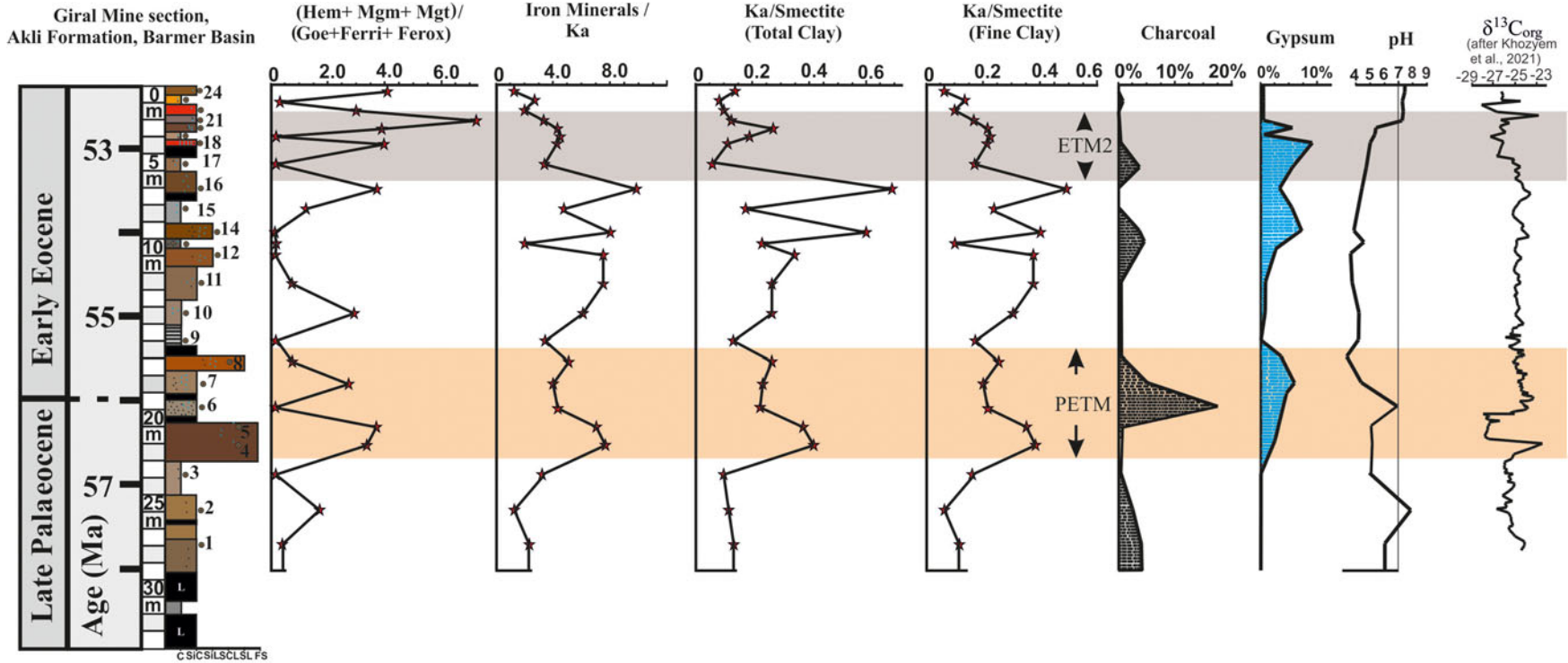
Figure 11. Depth-wise distribution of iron oxide ratios (hematite + maghemite + magnetite)/(goethite + ferrihydrite + feroxyhyte), iron oxide/Ka ratios and Ka/Sm ratios in the TC and FC fractions, charcoal fragments and gypsum contents and pH in the 24 beds of the Giral lignite mine section. The clay mineralogy from this study is also compared with the $\delta^{13}C_{org}$ curve of the section from Khozyem *et al.* (2021), demonstrating the correspondence with the Ka pulse and CIE in the Akli Formation sediments.
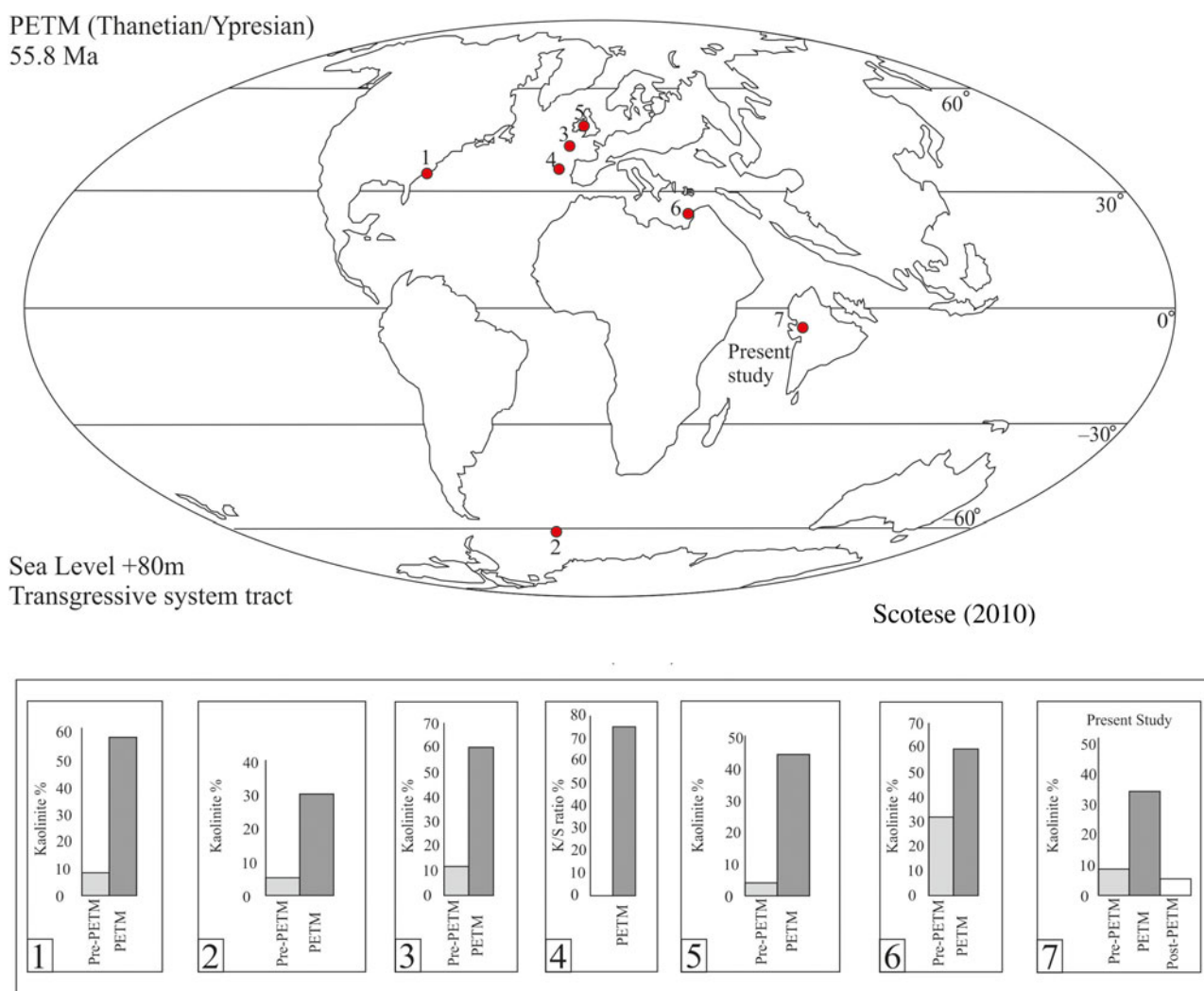
Figure 12. Global paleogeography during the PETM (Thanetian/Ypresian) at 55.8 Ma with important locations where Ka pulses during the PETM have been reported together with the present study of the Giral lignite mine section, Akli Formation, Barmer Basin, on the PETM map (modified after Scotese, 2010). This highlights six locations during the PETM: 1 = New Jersey Formation (after Gibson *et al.*, 1993); 2 = ODP site 690B (after Robert & Kennet., 1992); 3 = north-western Europe (after Knox, 1996; Kemp *et al.*, 2016); 4 = Zumaria Series, north Spain (after Gawenda *et al.*, 1999); 5 = North Sea Basin (after Walters *et al.*, 2022); 6 = southern Tethys Sea (after Bolle & Adatte, 2001). In addition, 7 = present study of the Giral mine section, India.

The abundant iron oxide minerals and red-coloured sediments during the Ka pulse in the Akli Formation can be explained through the dissolution kinetics of the Sm. The dissolution kinetics of the Sm-rich bentonite under acidic conditions is characterized by the release of Si, Al, Mg, Ca, Na and Fe from initial rapid to later slow rates from interlayer, tetrahedral and octahedral sheets of the Sm during its transformation into a 1:1 layer silicate (Metz *et al.*, 2005; Rozalén *et al.*, 2008; Marty *et al.*, 2011; Robin *et al.*, 2016). The release of interlayer cations is highly non-stoichiometric, while the release of Al, Si and Mg is stoichiometric. The release of Fe from octahedral sheets is comparable to the release of Al and Mg, but it occurs at a slower rate. However, a larger amount of Fe than expected after the dissolution was observed, which was explained due to the re-precipitation of Fe as hematite and goethite (Metz *et al.*, 2005). The presence of abundant Fe as iron oxide minerals supports the relative mobility of the major elements during weathering of the igneous rocks under ambient conditions in the following order: Ca > Na> Mg > K > Si > Fe > Al > Ti (Polynov, 1937; Anderson & Hawkes,

1958; Lasaga *et al.*, 1994). The Fe released during the decomposition of the primary minerals is quite immobile, forms stable iron oxides/oxyhydroxides such as ferrihydrite, goethite and hematite and causes the reddish colour in soils and sediments (Birkeland, 1999; Churchman, 2000). This explains why the Ka pulses during the PETM and ETM2 in the Akli Formation are accompanied by large amounts of iron oxide minerals and red-coloured sediments (Fig. 2 & Table 1). This is consistent with weathering under humid, tropical conditions marked by intense chemical weathering of the primary minerals, accounting for the large amounts of iron oxides in these soils and sediments (Kronberg *et al.*, 1982; Chandran *et al.*, 2005; Simas *et al.*, 2005; Morón *et al.*, 2013).

It is suggested that warming and wetting resulted in the large-scale transformation of the Sm along with the release of great amounts of Fe that formed iron oxide minerals (Figs 4 & 5 & Table 2). This is consistent with the greater concentration of iron oxide minerals in P–E transition palaeosols from the Bogota Basin of Colombia due to the increased rate of weathering and pedogenesis (Morón *et al.*, 2013). The anomalously high

concentrations of fine-grained iron oxide minerals at the P–E boundary sediments of Wilson Lake, New Jersey, also provide evidence for increased chemical weathering during the PETM, which resulted in the greater production of iron oxides in these sediments (Lippert & Zachos, 2007).

Forest fires and charcoal during the PETM in the palaeotropics

The unusually high proportion of charcoal in sediments of the Akli Formation during the P–E transition is related to large-scale forest wildfires. This finds support from the great amounts of charcoal fragments in the PETM sediments across the globe due to repeated fires at local to regional scales as an environmental response to warming during the hyperthermals (Scott, 2000; Crosdale, *et al.*, 2002; Kurtz *et al.*, 2003; Collinson, *et al.*, 2007). For example, unusually high concentrations of macroscopic charcoal fragments in the Cobham Lignite of England are consistent with the CIE at the P–E boundary (Scott, 2000; Collinson, 2001, Collinson *et al.*, 2003). In addition, some of the Palaeocene Russian coals are also unusually rich in charcoal, suggesting wildfires due to warming (Crosdale *et al.*, 2002). To test the wildfire hypothesis at the PETM, two Ocean Drilling Program (ODP) cores with a continuous PETM record from the Bass River site (ODP, Leg 174AX), New Jersey Margin, and Shatsky Rise (ODP 1210B) were explored to understand the causal relationship underlying the charcoal at the P–E boundary (Moore & Kurtz, 2008). Both sites show an unusually large amount of charcoal fragments in sediments, consistent with the CIE during the PETM (Moore & Kurtz, 2008). It was concluded that biomass burning was an environmental response to increased temperatures during the PETM and not the reason for the PETM (Moore & Kurtz, 2008).

The abrupt appearance of macroscopic charcoal fragments in lower parts of the section at amounts of ∼20% in sediments of the Akli Formation is consistent with the Ka pulse at the PETM (Figs 2 & 11). The charcoal again appears (5–7%) in upper parts of the section during the subsequent ETM2 hyperthermal (Figs 2 & 11). The presence of charcoal in this near-equatorial location during the P–E transition supports the notion that widespread wildfires were caused by unusual warming during the PETM and subsequent ETM2. The large amounts of charcoal fragments during the PETM and ETM2 are also consistent with the reports of 10–20% inertinite in the Early Palaeogene lignites of Gujrat and Rajasthan, western India (Rajak *et al.*, 2019). The large amounts of charcoal in the Early Palaeogene lignites of western India are comparable with those of the southern England, New Jersey and Schoningen lignites that characterise the PETM event at the global level (Scott, 2000; Crosdale *et al.*, 2002; Kurtz *et al.*, 2003; Collinson *et al.*, 2007; Robson *et al.*, 2015).

Conclusions

This study provides the clay mineral evidence regarding the PETM and subsequent ETM2 hyperthermals from a near-equatorial region represented by the Akli Formation of Barmer Basin, India. The 32 m-thick P–E transition sediments in this near-equatorial location are characterized by abrupt changes in the abundance of Sm and Ka. It is also characterized by a 3–4-fold increase (from 5–10% to 25–35%) of Ka in sediments during the P–E transition in comparison to pre-P–E and post-P–E transition sediments. The Ka pulse was caused by warming (3–5°C), increased precipitation (25–50%) and increased chemical weathering in the near-equatorial region. However, the Sm, which formed after rhyolite weathering, is marked by an abrupt decrease from 90% to 60% during the P–E transition compared to pre-P–E and post-P–E transition sediments. The acid-weathering conditions during the P–E transition in the equatorial region resulted in a large-scale transformation of the Sm into Ka. Dissolution of the Sm during the P–E hyperthermals resulted in the formation of iron oxide minerals and red- to deep red-coloured sediments. The abrupt appearance of unusually large amounts (∼20%) of macroscopic charcoal fragments in these sediments is consistent with the Ka pulse during the P–E transition and confirms wildfire activity in the near-equatorial regions, supporting unusual warming and the widespread wildfire hypothesis during the PETM. The Ka pulse, dissolution of Sm under acid-weathering conditions and the wildfire evidence from Akli Formation sediments are consistent with the CIEs of the Barmer Basin and the global reference curves. Thus, the Akli Formation sediments deposited during the P–E transition represent an important terrestrial archive of near-equatorial PETM and ETM2 conditions.

References

Anand R., Gilkes R., Armitage T. & Hillyer J. (1985) Feldspar weathering in lateritic saprolite. *Clays and Clay Minerals*, **33**, 31–43.

Anderson D. & Hawkes H. (1958) Relative mobility of the common elements in weathering of some schist and granite areas. *Geochimica et Cosmochimica Acta*, **14**, 204–210.

Arambourg C. (1952) Les vertébrés fossiles des gisements de phosphates (Maroc-Algérie-Tunisie). *Notes et Mémoires du Service géologique du Maroc*, **92**, 1–372.

Barnhisel R.I. & Bertsch P.M. (1989) Chlorites and hydroxy-interlayered vermiculite and smectite. *Minerals in Soil Environments*, **1**, 729–788.

Bhattacharyya T., Pal D. & Deshpande, S. (1993) Genesis and transformation of minerals in the formation of red (Alfisols) and black (Inceptisols and Vertisols) soils on Deccan basalt in the Western Ghats, India. *Journal of Soil Science*, **44**, 159–171.

Birkeland P.W. (1999) *Soils and Geomorphology*, 3rd edition. Oxford University Press, New York, NY, USA, 448 pp.

Biswas S. (1982) Rift basins in western margin of India and their hydrocarbon prospects with special reference to Kutch basin. *AAPG Bulletin*, **66**, 1497–1513.

Bladon A.J., Clarke S.M. & Burley S.D. (2015) Complex rift geometries resulting from inheritance of pre-existing structures: Insights and regional implications from the Barmer Basin rift. *Journal of Structural Geology*, **71**, 136–154.

Bolle M.P. & Adatte T. (2001) Palaeocene–Early Eocene climatic evolution in the Tethyan realm: clay mineral evidence. *Clay Minerals*, **36**, 249–261.

Cappetta H. (2012) *Handbook of Paleoichthyology, Vol. 3E: Chondrichthyes: Mesozoic and Cenozoic Elasmobranchii: Teeth*. Verlag Dr. Friedrich Pfeil, Munich, Germany, 512 pp.

Carmichael J.W., Inglis G.N., Badger M.P.S., Naafs B.D.A., Behrooz L., Remmelzwaal S. *et al.* (2017) Hydrological and associated biogeochemical consequences of rapid global warming during the Paleocene–Eocene Thermal Maximum. *Global Planetary Change*, **157**, 114–138.

Chaloner W.G. (1968) The palaeoecology of fossil spores. Pp. 125–138 in: *Evolution and Environment* (E.T. Drake, editor). Yale University Press, New Haven, CT, USA.

Chandran P., Ray S.K., Bhattacharyya T., Srivastava P., Krishnan P. & Pal, D.K. (2005) Lateritic soils of Kerala, India: their mineralogy, genesis, and taxonomy. *Australian Journal of Soil Research*, **43**, 839–852.

Chitale D. & Gueven N. (1989) Weathering of Deccan trap basalts in western India. *Clay Research*, **8**, 67–83.

Choudhury T.R., Banerjee S., Khanolkar S., Saraswati P.K. & Meena, S.S. (2021) Glauconite authigenesis during the onset of the Paleocene–Eocene Thermal Maximum: a case study from the Khuiala Formation in Jaisalmer Basin, India. *Palaeogeography, Palaeoclimatology, Palaeoecology*, **571**, 1–20.

Churchman G. (2000) The alteration and formation of soil minerals by weathering. Pp. F3–F76 in: *Handbook of Soil Science* (M.E. Summer, editor). CRC Press, Boca Raton, FL, USA.

Clechenko E.R., Kelly D.C., Harrington G.J. & Stiles C.A. (2007) Terrestrial records of a regional weathering profile at the Paleocene–Eocene boundary in the Williston Basin of North Dakota. *Geological Society of America Bulletin*, **119**, 428–442.

Collinson M.E. (2001) Cainozoic ferns and their distribution. *Brittonia*, **53**, 173–235.

Collinson M.E., Hooker J.J. & Groecke, D.R. (2003) Cobham lignite bed and penecontemporaneous macrofloras of southern England: a record of vegetation and fire across the Paleocene–Eocene Thermal Maximum, in: Causes and Consequences of Globally Warm Climates in the Early Paleogene. *Special Paper Geological Society of America*, **369**, 333–349.

Collinson M.E., Steart D., Scott A., Glasspool I. & Hooker J. (2007). Episodic fire, runoff and deposition at the Palaeocene–Eocene boundary. *Journal of the Geological Society*, **164**, 87–97.

Compton P.M. (2009) The geology of the Barmer Basin, Rajasthan, India, and the origins of its major oil reservoir, the Fatehgarh Formation. *Petroleum Geoscience*, **15**, 117–130.

Cramer B.S. Aubry M.P., Miller K.G., Olsson RK., Wright J.D. & Kent, D.V. (1999) An exceptional chronologic, isotopic, and clay mineralogic record of the latest Paleocene thermal maximum, Bass River, NJ, ODP 174AX. *Bulletin de la Société géologique de France*, **170**, 883–897.

Crosdale P.J., Sorokin A.P., Woolfe K.J. & Macdonald D.I.M. (2002) Inertinite-rich Tertiary coals from the Zeya–Bureya Basin, far eastern Russia. *International Journal of Coal Geology*, **51**, 215–235.

Cui Y., Kump L.R., Ridgwell A.J., Charles A.J., Junium C.K., Diefendorf A.F. *et al.* (2011) Slow release of fossil carbon during the Palaeocene–Eocene Thermal Maximum. *Nature Geoscience*, **4**, 481–485.

Dasgupta S. (1974) The stratigraphy of the west Rajasthan shelf. Pp. 219–233 in: *Proceedings of IV Colloquium on Indian Micropalaeontology and Stratigraphy* (B.S. Venkatachala and V.V. Sastri, editors). Institute of Petroleum Exploration, Oil and Natural Gas Commissions, Dehradun, Inda.

De Kimpe C., Gastuche M. & Brindley G.W. (1961) Ionic coordination in alumino-silicic gels in relation to clay mineral formation. *American Mineralogist*, **46**, 1370–1381.

Delvaux B., Herbillon A.J., Vielvoye L. & Mestdagh M. (1990) Surface properties and clay mineralogy of hydrated halloysitic soil clays. II: Evidence for the presence of halloysite/smectite (H/Sm) mixed-layer clays. *Clay Minerals*, **25**, 141–160.

Dickens G.R., O'Neil J.R., Rea D.K. & Owen R.M. (1995) Dissociation of oceanic methane hydrate as a cause of the carbon isotope excursion at the end of the Paleocene. *Paleoceanography*, **10**, 965–971.

Dickens G.R., Castillo M.M. & Walker J.C. (1997) A blast of gas in the latest Paleocene: simulating first-order effects of massive dissociation of oceanic methane hydrate. *Geology*, **25**, 259–262.

Dietel J., Ufer K., Kaufhold S. & Dohrmann R. (2019) Crystal structure model development for soil clay minerals – II. Quantification and characterization of hydroxy-interlayered smectite (HIS) using the Rietveld refinement technique. *Geoderma*, **347**, 1–12.

Do Campo M., Bauluz B., Del Papa C., White T., Yuste A. & Mayayo M.J. (2018) Evidence of cyclic climatic changes recorded in clay mineral assemblages from a continental Paleocene–Eocene sequence, northwestern Argentina. *Sedimentary Geology*, **368**, 44–57.

Ebert D.A. & Stehmann M.F. (2013) *Sharks, Batoids, and Chimaeras of the North Atlantic*. FAO Species Catalogue for Fishery Purposes 7. FAO, Rome, Italy, 524 pp.

Eby G.N. & Kochhar N. (1990) Geochemistry and petrogenesis of the Malani Igneous Suite, peninsular India. *Journal Geological Society of India*, **36**, 109–130.

Elling F.J., Gottschalk J., Doeana K.D., Kusch S., Hurley S.J. & Pearson A. (2019) Archaeal lipid biomarker constraints on the Paleocene–Eocene carbon isotope excursion. *Nature Communications*, **10**, 1–10.

Frieling J., Reichart G.J., Middelburg J.J., Röhl U., Weterhold T., Bohaty S.M. & Sluijs A. (2018) Tropical Atlantic climate and ecosystem regime shifts during the Paleocene–Eocene Thermal Maximum. *Climate of the Past*, **14**, 39–55.

Frieling J., Gebhardt H., Huber M., Adekeye O.A., Akande S.O., Reichart G.J. *et al.* (2017) Extreme warmth and heat-stressed plankton in the tropics during the Paleocene–Eocene Thermal Maximum. *Science Advances*, **3**, 1–9.

Gawenda P., Winkler W., Schmitz B. & Adatte, T. (1999) Climate and bioproductivity control on carbonate turbidite sedimentation (Paleocene to earliest Eocene, Gulf of Biscay, Zumaia, Spain). *Journal of Sedimentary Research*, **69**, 1253–1261.

Gibson T.G., Bybell L.M. & Owens J.P. (1993) Latest Paleocene lithologic and biotic events in neritic deposits of southwestern New Jersey. *Paleoceanography*, **8**, 495–514.

Gibson T.G., Bybell L.M. & Mason D.B. (2000) Stratigraphic and climatic implications of clay mineral changes around the Paleocene/Eocene boundary of the northeastern US margin. *Sedimentary Geology*, **134**, 65–92.

Gilkes R. & Suddhiprakran A. (1979) Biotite alteration in deeply weathered granite. I. Morphological, mineralogical, and chemical properties. *Clays and Clay Minerals*, **27**, 349–360.

Gjems O. (1967) Studies on clay minerals and clay-mineral formation in soil profiles in Scandinavia. *Med. Nor. Skogforksvesen*, **21**, 303–415.

Gombos A.M. Jr, Powell W.G. & Norton I.O. (1995) The tectonic evolution of western India and its impact on hydrocarbon occurrences: an overview. *Sedimentary Geology*, **96**, 119–129.

Gregory L.C., Meert J.G., Bingen B., Pandit M.K. & Torsvik T.H. (2009) Paleomagnetism and geochronology of the Malani Igneous Suite, northwest India: implications for the configuration of Rodinia and the assembly of Gondwana. *Precambrian Research*, **170**, 13–26.

Grim R.E. & Güven N. (1978) *Bentonites: Geology, Minerlaogy, Properties and Uses*. Developents in Sedimentlogy 24. Elsevier, Amsterdams, The Netherlands, 267 pp.

Gupta S. & Kumar K. (2019) Precursors of the Paleocene–Eocene Thermal Maximum (PETM) in the Subathu Group, NW sub-Himalaya, India. *Journal of Asian Earth Sciences*, **169**, 21–46.

Handley L., O'Halloran A., Pearson P.N., Hawkins E., Nicholas C.J., Schouten S. *et al.* (2012) Changes in the hydrological cycle in tropical East Africa during the Paleocene–Eocene Thermal Maximum. *Palaeogeography, Palaeoclimatology, Palaeoecology*, **329**, 10–21.

Harriss R.C. & Adams J.A. (1966) Geochemical and mineralogical studies on the weathering of granitic rocks. *American Journal of Science*, **264**, 146–173.

Herbillon A., Frankart R. & Vielvoye L. (1981) An occurrence of interstratified kaolin–smectite minerals in a red-black soil toposequence. *Clay Minerals*, **16**, 195–201.

Inglis G.N., Bragg F., Burls N.J., Cramwinckel M.J., Evans D., Foster G.L. *et al.* (2020). Global mean surface temperature and climate sensitivity of the Early Eocene Climatic Optimum (EECO), Paleocene–Eocene Thermal Maximum (PETM), and latest Paleocene. *Climate of the Past*, **16**, 1953–1968.

Jackson M. (1975) *Soil Chemical Analysis – Advanced Course*, 10th printing. Published by author, Department of Soil Science, University of Wisconsin, Madison, WI, USA, 930 pp.

Jackson M. (1979) *Soil Chemical Analysis – Advanced Course*, 11th printing. Published by author, Department of Soil Science, University of Wisconsin, Madison, WI, USA, 930 pp.

Jaramillo C. (2002) Response of tropical vegetation to Paleogene warming. *Paleobiology*, **28**, 222–243.

Jaramillo C., Ochoa D., Contreras L., Pagani M., Carvajal-Ortiz H., Pratt L.M. et al. (2010) Effects of rapid global warming at the Paleocene–Eocene boundary on neotropical vegetation. *Science*, **330**, 957–961.

Ji K., Wang C., Hong H., Yin K., Zhao C., Xu Y. et al. (2023) Elevated physical weathering exceeds chemical weathering of clays during the Paleocene–Eocene Thermal Maximum in the continental Bighorn Basin (Wyoming, USA). *Palaeogeography, Palaeoclimatology, Palaeoecology*, **615**, 111445.

Kapoor B. (1972) Weathering of micaceous clays in some Norwegian podzols. *Clay Minerals*, **9**, 383–394.

Kemp S.J., Ellis M.A., Mounteney I. & Kender S. (2016) Paleoclimatic implications of high-resolution clay mineral assemblages preceding and across the onset of the Palaeocene–Eocene Thermal Maximum, North Sea Basin. *Clay Minerals*, **51**, 793–813.

Kennett J.P. & Scott, L. (1991) Abrupt deep-sea warming, palaeoceanographic changes and benthic extinctions at the end of the Palaeocene. *Nature*, **353**, 225–229.

Khanolkar S. & Sharma J. (2019) Record of Early to Middle Eocene paleoenvironmental changes from lignite mines, western India. J*ournal of Micropalaeontology*, **38**, 1–24.

Khozyem H., Adatte T., Keller G. & Spangenberg J. E. (2021) Organic carbon isotope records of the Paleocene–Eocene thermal maximum event in India provide new insights into mammal origination and migration. *Journal of Asian Earth Sciences*, **212**, 104736.

Knight J.L., Cicimurri D.J. & Purdy R.W. (2007) New Western Hemisphere occurrences of Schizorhiza Weiler, 1930 and Eotorpedo White, 1934 (Chondrichthyes, Batomorphii). *Paludicola*, **6**, 87–93.

Knox R.W.O. (1996) Correlation of the early Paleogene in northwest Europe: an overview. *Geological Society, London, Special Publication*, **101**, 1–11.

Koch P.L., Zachos J.C. & Gingerich P.D. (1992) Correlation between isotope records in marine and continental carbon reservoirs near the Palaeocene/Eocene boundary. *Nature*, **358**, 319–322.

Kristo C., Rahardjo H. & Satyanaga A. (2017) Effects of variations in rainfall intensity on slope stability in Singapore. *International Soil and Water Conservation Research*, **5**, 258–264.

Kronberg B.I., Fyfe W.S., McKinnon B.J., Couston J.F., Filho B.S. & Nash R.A. (1982) Model for bauxite formation: Paragominas (Brazil). *Chemical Geology*, **35**, 311–320.

Kurtz A.C., Kump L.R., Arther M.A., Zachos J.C. & Paytan A. (2003) Early Cenozoic decupling of the global carbon and sulfur cycles. *Paleoceanography*, **18**, 1–14.

Lasaga A.C., Soler J.M., Ganor J., Burch T.E. & Nagy K.L. (1994) Chemical weathering rate laws and global geochemical cycles. *Geochimica et Cosmochimica Acta*, **58**, 2361–2386.

Lippert P.C. & Zachos J.C. (2007) A biogenic origin for anomalous fine-grained magnetic material at the Paleocene–Eocene boundary at Wilson Lake, New Jersey. *Paleoceanography*, **22**, 1–8.

Maheshwari A., Sial A., Coltorti M., Chittora V. & Cruz, M.J. (2001) Geochemistry and petrogenesis of Siwana peralkaline granites, west of Barmer, Rajasthan, India. *Gondwana Research*, **4**, 87–95.

Marty N.C., Cama J., Sato T., Chino D., Villiéras F., Razafitianamaharavo A. et al. (2011) Dissolution kinetics of synthetic Na-smectite. An integrated experimental approach. *Geochimica et Cosmochimica Acta*, **75**, 5849–5864.

McInerney F.A. & Wing S.L. (2011) The Paleocene–Eocene Thermal Maximum: a perturbation of carbon cycle, climate, and biosphere with implications for the future. *Annual Review of Earth and Planetary Sciences*, **39**, 489–516.

Meng M., Zhang J., Wong Y.D. & Au, P.H. (2016) Effect of weather conditions and weather forecast on cycling travel behaviour in Singapore. *International Journal of Sustainable Transportation*, **10**, 773–780.

Metz V., Raanan H., Pieper H., Bosbach D. & Ganor J. (2005) Towards the establishment of a reliable proxy for the reactive surface area of smectite. *Geochimica et Cosmochimica Acta*, **69**, 2581–2591.

Moore E.A. & Kurtz A.C. (2008) Black carbon in Paleocene–Eocene boundary sediments: a test of biomass combustion as the PETM trigger. *Palaeogeography, Palaeoclimatology, Palaeoecology*, **267**, 147–152.

Morley R.J. (2000) *Origin and Evolution of Tropical Rain Forests*. John Wiley & Sons, Hoboken, NJ, USA, 362 pp.

Morón S., Fox D.L., Feinberg J.M., Jaramillo C., Bayona G., Montes C. & Bloch, J.I. (2013) Climate change during the Early Paleogene in the Bogotá Basin (Colombia) inferred from paleosol carbon isotope stratigraphy, major oxides, and environmental magnetism. *Palaeogeography, Palaeoclimatology, Palaeoecology*, **388**, 115–127.

Murphy B., Farley K. & Zachos J. (2010) An extra-terrestrial ³He-based time-scale for the Paleocene–Eocene Thermal Maximum (PETM) from Walvis Ridge, IODP Site 1266. *Geochimica et Cosmochimica Acta*, **74**, 5098–5108.

Nagori M. & Khosla S. (2019) Early Eocene Ostracoda from the Akli Formation of Barmer Basin, Rajasthan. *Journal of Palaeontological Society of India*, **64**, 11–26.

Naskar P. & Baksi S.K. (1976) Palynological investigation of Akli lignite, Rajasthan. *Palaeontologist*, **25**, 314–319.

Nesbitt H.W. (1977) Estimation of the thermodynamic properties of Na-, Ca- and Mg-beidellites. *The Canadian Mineralogist*, **15**, 22–30.

Nesbitt H.W. & Young G.M. (1984) Prediction of some weathering trends of plutonic and volcanic rocks based on thermodynamic and kinetic considerations. *Geochimica et Cosmochimica Acta*, **48**, 1523–1534.

Nichols G. (2009) *Sedimentology and Stratigraphy*, 2nd edition, Wiley-Blackwell, Hoboken, NJ, USA, 419 pp.

Norrish K. & Pickering J. (1983) Clay minerals. Pp. 282–308 in: *Soils: An Australian Viewpoint*. Academic Press, London, UK.

Noubhani A. & Cappetta H. (1997) Les Orectolobiformes, Carcharhiniformes et Myliobatiformes des bassins a phosphate du Maroc (Maastrichtien-Lutetien basal). *Palaeo Ichthyologica*, **8**, 1–327.

Pagani M., Pedentchouk N., Huber M., Sluijs A., Schouten S., Brinkhuis H. et al. (2006) Arctic hydrology during global warming at the Palaeocene/Eocene thermal maximum. *Nature*, **442**, 671–675.

Pal D.K. & Deshpande S.B. (1987) Characteristics and genesis of minerals in some benchmark Vertisols of India. *Pedologie*, **37**, 259–275.

Pal D.K., Deshpande S.B., Venugopal K. & Kalbande A. (1989) Formation of di- and trioctahedral smectite as evidence for paleoclimatic changes in southern and central peninsular India. *Geoderma*, **45**, 175–184.

Pareek H.S. (1981) Basin configuration and sedimentary stratigraphy of western Rajasthan. *Journal Geological Society of India*, **22**, 517–527.

Pareek H.S. (1984) Pre-Quaternary geology and mineral resources of north-western Rajasthan. *Memoirs of the Geological Survey of India*, **115**, 1–107.

Pocknall D.T., Clowes C.D. & Jarzen D.M. (2022) *Spinizonocolpites prominatus* (McIntyre) Stover & Evans: fossil *Nypa* pollen, taxonomy, morphology, global distribution, and paleoenvironmental significance. *New Zealand Journal of Geology and Geophysics*, 10.1080/00288306.2022.2078376.

Polynov B.B. (1937) *The Cycle of Weathering* (translated from the Russian by A. Muir, W.G. Ogg & T. Murby). Thomas Murby and Company, London, UK.

Prasad V., Farooqui A., Tripathi M., Garg R. & Thakur B. (2009) Evidence of late Palaeocene–Early Eocene equatorial rain forest refugia in southern Western Ghats, India. *Journal of Biosciences*, **34**, 777–794.

Prasad V., Uddandam P.R., Agrawal S., Bajpai S., Singh I., Mishra A.K. et al. (2020) Biostratigraphy, palaeoenvironment and sea level changes during pre-collisional (Palaeocene) phase of the Indian plate: palynological evidence from Akli Formation in Giral Lignite Mine, Barmer Basin, Rajasthan, Western India. *Episodes*, **43**, 476–488.

Rajak P.K., Singh V.K. & Singh P.K. (2019) Distribution of Inertinites in the early Paleogene lignites of western India: on the possibility of wildfire activities. *Journal of the Geological Society of India*, **93**, 523–532.

Rajkumari P. & Prasad G.V.R. (2020) New chondrichthyan fauna from the Palaeogene deposits of Barmer district, Rajasthan, western India: age, palaeoenvironment and intercontinental affinities. *Geobios*, **58**, 55–72.

Rana R., Kumar K., Singh H. & Rose K. (2005) Lower vertebrates from the late Palaeocene–earliest Eocene Akli Formation, Giral lignite mine, Barmer District, western India. *Current Science*, **89**, 1606–1613.

Rana R., Kumar K. & Singh H. (2006) Palaeocene vertebrate fauna from the Fatehgarh Formation of Barmer district, Rajasthan, western India. Pp.

113–130 in: *Micropalaeontology: Application in Stratigraphy and Paleoceanography* (D.K. Sinha, editor). Narosa Publishing House, New Delhi, India.

Rengasamy P., Sarma V., Murthy R. & Murti G.K. (1978) Mineralogy, genesis and classification of ferruginous soils of the eastern Mysore Plateau, India. *Journal of Soil Science*, **29**, 431–445.

Robert C. & Kennett J.P. (1992) Paleocene and Eocene kaolinite distribution in the South Atlantic and Southern Ocean: Antarctic climatic and paleoceanographic implications. *Marine Geology*, **103**, 99–110.

Robert C. & Kennett J.P. (1994) Antarctic subtropical humid episode at the Paleocene–Eocene boundary: clay-mineral evidence. *Geology*, **22**, 211–214.

Robert C. & Kennett J.P. (1997) Antarctic continental weathering changes during Eocene–Oligocene Cryosphere Expansion: clay mineral and oxygen isotope evidence. *Geology*, **25**, 587–590.

Robin V., Tertre E., Regnault O. & Descostes M. (2016) Dissolution of beidellite in acidic solutions: ion exchange reactions and effect of crystal chemistry on smectite reactivity. *Geochimica et Cosmochimica Acta*, **180**, 97–108.

Robson B.E., Collinson M.E., Riegel W., Wilde V., Scott A.C. & Pancost R.D. (2015) Early Paleogene wildfires in peat-forming environments at Schöningen, Germany. *Palaeogeography, Palaeoclimatology, Palaeoecology*, **437**, 53–62.

Röhl U., Westerhold T., Bralower T.J. & Zachos J.C. (2007) On the duration of the Paleocene–Eocene Thermal Maximum (PETM). *Geochemistry, Geophysics, Geosystems*, **8**, 1–13.

Rose K.D., Smith T., Rana R.S., Sahni A., Singh H., Missiaen P. & Folie A. (2006) Early Eocene (Ypresian) continental vertebrate assemblage from India, with description of a new anthracobunid (Mammalia, Tethytheria). *Journal of Vertebrate Palaeontology*, **26**, 219–225.

Rozalén M.L., Huertas F.J., Brady P.V., Cama J., García-Palma S. & Linares J. (2008) Experimental study of the effect of pH on the kinetics of montmorillonite dissolution at 25°C. *Geochimica et Cosmochimica Acta*, **72**, 4224–4253.

Rush W.D., Kiehl J.T., Shields C.A. & Zachos J.C. (2021) Increased frequency of extreme precipitation events in the North Atlantic during the PETM: observations and theory. *Palaeogeography, Palaeoclimatology, Palaeoecology*, **568**, 110289.

Samanta A., Bera M., Ghosh R., Bera S., Filley T., Pande K. et al. (2013) Do the large carbon isotopic excursions in terrestrial organic matter across Paleocene–Eocene boundary in India indicate intensification of tropical precipitation? *Palaeogeography, Palaeoclimatology, Palaeoecology*, **387**, 91–103.

Schouten S., Woltering M., Rijpstra W.I.C., Sluijs A., Brinkhuis H. & Damsté J.S.S. (2007) The Paleocene–Eocene carbon isotope excursion in higher plant organic matter: differential fractionation of angiosperms and conifers in the Arctic. *Earth and Planetary Science Letters*, **258**, 581–592.

Scotese C. (2010) *The PALEOMAP Project PaleoAtlas for ArcGIS, vol. 1: Cenozoic Paleogeographic and Plate Tectonic Reconstructions*. PALEOMAP Project, Arlington, TX, USA.

Scott A.C. (2000) The pre-Quaternary history of fire. *Palaeogeography, Palaeoclimatology, Palaeoecology*, **164**, 281–329.

Secord R., Gingerich P.D., Lohmann K.C. & MacLeod K.G. (2010) Continental warming preceding the Palaeocene–Eocene Thermal Maximum. *Nature*, **467**, 955–958.

Simas F.N.B., Schaefer C.E.G.R., Fernandes Filho E.I., Chagas A.C. & Brandão P.C. (2005) Chemistry, mineralogy and micropedology of highland soils on crystalline rocks of Serra da Mantiqueira, southeastern Brazil. *Geoderma*, **125**, 187–201.

Singh H. (2015) Palynofloral investigation of the Akli Formation (Palaeocene) of Giral lignite mine, Barmer district, Rajasthan. *Geophytology*, **45**, 209–214.

Sisodia M.S. & Singh, U.K. (2000) Depositional environment and hydrocarbon prospects of the Barmer Basin, Rajasthan, India. *Nafta (Zagreb)*, **51**, 309–326.

Smith F.A., Wing S.L. & Freeman K.H. (2007) Magnitude of the carbon isotope excursion at the Paleocene–Eocene Thermal Maximum: the role of plant community change. *Earth and Planetary Science Letters*, **262**, 50–65.

Smith T., Kumar K., Rana R.S., Folie A., Solé F., Noiret C. et al. (2016) New Early Eocene vertebrate assemblage from western India reveals a mixed fauna of European and Gondwana affinities. *Geoscience Frontiers*, **7**, 969–1001.

Sreenivasan S.P., Bera M.K., Samanta A. & Vadlamani R. (2018) Palaeocene–Eocene carbon isotopic excursion from the shallow-marine-carbonate sequence of northeast India: implications on the CIE magnitude and geometry. *Journal of Earth System Science*, **127**, 1–11.

Srivastava P., Parkash B. & Pal D.K. (1998) Clay minerals in soils as evidence of Holocene climatic change, central Indo-Gangetic Plains, north-central India. *Quaternary Research*, **50**, 230–239.

Stow D.A.V. (2005) *Sedimentary Rocks in the Field: A Color Guide*. Manson Publishing, London, UK, 320 pp.

Tabaei M. & Singh R.Y. (2002) Palaeoenvironment and palaeoecological significance of microforaminiferal linings in the Akli Lignite, Barmer Basin, Rajasthan, India. *Iranian International Journal of Science*, **3**, 263–277.

Tardy Y., Bocquier G., Paquet H. & Millot G. (1973) Formation of clay from granite and its distribution in relation to climate and topography. *Geoderma*, **10**, 271–284.

Tateo F. (2020) Clay minerals at the Paleocene–Eocene Thermal Maximum: interpretations, limits, and perspectives. *Minerals*, **10**, 1073.

Torsvik T.H., Van der Voo R., Preeden U., Mac Niocaill C., Steinberger B., Doubrovine P.V. et al. (2012) Phanerozoic polar wander, palaeogeography and dynamics. *Earth-Science Reviews*, **114**, 325–368.

Tripathi S. (1993) New angiosperm pollen from subsurface early Palaeogene sediments of Barmer district, Rajasthan, India. *Journal of Palaeosciences*, **42**, 61–65.

Tripathi S. (1995) Palynology of subsurface Palaeocene–Eocene sediments near Kapurdi, Barmer district, Rajasthan, India. *Palaeobotanist*, **43**, 45–53.

Tripathi S. (1997) Palynological changes across subsurface Palaeocene–Eocene sediments at Barmer, Rajasthan, India. *Journal of Palaeosciences*, **46**, 168–171.

Tripathi S., Singh U. & Sisodia M. (2003) Palynological investigation and environmental interpretation on Akli Formation (Late Palaeocene) from Barmer Basin, western Rajasthan, India. *Journal of Palaeosciences*, **52**, 87–95.

Tripathi S., Kumar M. & Srivastava D. (2009) Palynology of lower Palaeogene (Thanetian–Ypresian) coastal deposits from the Barmer Basin (Akli Formation, western Rajasthan, India): palaeoenvironmental and paleoclimatic implications. *Geologica Acta*, **7**, 147–160.

Walters G.L., Kemp S.J., Hemingway J.D., Johnston D.T. & Hodell D.A. (2022) Clay hydroxyl isotopes show an enhanced hydrologic cycle during the Paleocene–Eocene Thermal Maximum. *Nature Communications*, **13**, 7885.

Wang C.W., Hong H.L., Song B.W., Yin K., Li Z.H., Zhang K.X. & Ji L. (2011) The Early-Eocene Climate Optimum (EECO) event in the Qaidam Basin, northwest China: clay evidence. *Clay Minerals*, **46**, 649–661.

Wang C., Adriaens R., Hong H., Elsen J., Vandenberghe N., Lourens L.J. et al. (2017) Clay mineralogical constraints on weathering in response to Early Eocene hyperthermal events in the Bighorn Basin, Wyoming (Western Interior, USA). *GSA Bulletin*, **129**, 997–1011.

Westerhold T., Röhl U., McCarren H.K. & Zachos J.C. (2009) Latest on the absolute age of the Paleocene–Eocene Thermal Maximum (PETM): new insights from exact stratigraphic position of key ash layers +19 and –17. *Earth and Planetary Science Letters*, **287**, 412–419.

Westerhold T., Marwan N., Drury A.J., Liebrand D., Agnini C., Anagnostou E. et al. (2020) An astronomically dated record of Earth's climate and its predictability over the last 66 million years. *Science*, **369**, 1383–1387.

White D.E., Hem J.D. & Waring G. (1963) *Chemical Composition of Subsurface Waters*. USGS Professional Paper 440-F. United States Geological Survey, Reston, VA, USA, 74 pp.

Wilson M. (1987) *A Handbook of Determinative Methods in Clay Mineralogy*. Blackie, Glasgow, UK, 308 pp.

Wilson M. & Cradwick P. (1972) Occurrence of interstratified kaolinite–montmorillonite in some Scottish soils. *Clay Minerals*, **9**, 435–437.

Wing S.L., Harrington G.J., Smith F.A., Bloch J.I., Boyer D.M. & Freeman K.H. (2005) Transient floral change and rapid global warming at the Paleocene–Eocene boundary. *Science*, **310**, 993–996.

Zachos J.C., Pagani M., Sloan L., Thomas E. & Billups K. (2001) Trends, rhythms, and aberrations in global climate 65 Ma to present. *Science*, **292**, 686–693.

Zachos J.C., Wara M.W., Bohaty S., Delaney M.L., Petrizzo M.R., Brill A. *et al.* (2003) A transient rise in tropical sea surface temperature during the Paleocene–Eocene Thermal Maximum. *Science*, **302**, 1551–1554.

Zachos J.C., Röhl U., Schellenberg S.A., Sluijs A., Hodell D.A., Kelly D.C. *et al.* (2005) Rapid acidification of the ocean during the Paleocene–Eocene Thermal Maximum. *Science*, **308**, 1611–1615.

Zachos J.C., Schouten S., Bohaty S., Quattlebaum T., Sluijs A., Brinkhuis H. *et al.* (2006) Extreme warming of mid-latitude coastal ocean during the Paleocene–Eocene Thermal Maximum: inferences from TEX86 and isotope data. *Geology*, **34**, 737.

Zeebe R.E., Zachos J.C. & Dickens G.R. (2009) Carbon dioxide forcing alone insufficient to explain Palaeocene–Eocene Thermal Maximum warming. *Nature Geoscience*, **2**, 576–580.

Zhao C., Wang C., Hong H., Algeo T.J., Yin K., Ji K. *et al.* (2021) Origin of dioctahedral smectites in Lower Eocene Lulehe Formation paleosols (Qaidam Basin, China). *Applied Clay Science* **203**, 106026.